Global Distribution and Characteristics of Diurnally Varying Low-Level Jets

DARAN L. RIFE, JAMES O. PINTO, ANDREW J. MONAGHAN, AND CHRISTOPHER A. DAVIS

National Center for Atmospheric Research, Boulder, Colorado*

JOHN R. HANNAN

Defense Threat Reduction Agency, Fort Belvoir, Virginia

(Manuscript received 12 November 2009, in final form 4 May 2010)

ABSTRACT

This study documents the global distribution and characteristics of diurnally varying low-level jets (LLJs), including their horizontal, vertical, and temporal structure, with a special emphasis on highlighting the underlying commonalities and unique qualities of the various nocturnal jets. Two tools are developed to accomplish this goal. The first is a 21-yr global reanalysis performed with the fifth-generation Pennsylvania State University–NCAR Mesoscale Model (MM5) using a horizontal grid spacing of 40 km. A unique characteristic of the reanalysis is the availability of hourly three-dimensional output, which permits the full diurnal cycle to be analyzed. Furthermore, the horizontal grid spacing of 40 km better resolves many physiographic features that host LLJs than other widely used global reanalyses. This makes possible a detailed examination of the systematic onset and cessation of the jets, including time–height representations of the diurnal cycle. The second tool is an index of nocturnal LLJ (NLLJ) activity based upon the vertical structure of the wind's temporal variation, where the temporal variation is defined in local time. The first available objectively constructed global maps of recurring NLLJs are created from this index, where the various NLLJs can be simultaneously viewed at or near their peak time. These maps not only highlight all of the locations where NLLJs are known to recur, but they also reveal a number of new jets.

The authors examine the basic mechanisms that give rise to the NLLJs identified in four disparate locations, each having a profound influence on the regional climate. The first, the extensively studied Great Plains NLLJ, is used to confirm the veracity of the global analysis and the index of NLLJ activity. It also provides context for three of the many newly identified NLLJs: 1) Tarim Pendi in northwest China; 2) Ethiopia in eastern Africa; and 3) Namibia–Angola in southwest Africa. Jets in these four regions illustrate the variety of physiographic and thermal forcing mechanisms that can produce NLLJs.

1. Introduction

Worldwide, a central influence on human activity is rainfall that derives from transport of water vapor from low to high latitudes or directly from warm oceans inland over continents. Much of this transport occurs in confined wind corridors termed generically as low-level jets (LLJs). As outlined in the review by Stensrud (1996, hereafter S96), these jets take many forms. In extratropical cyclones, atmospheric rivers have been identified (Newell et al. 1992; Ralph et al. 2004, 2005) in which water vapor is rapidly transported to higher latitudes, often encountering pronounced coastal orography where flooding rains can occur (e.g., Smith et al. 2009; Neiman et al. 2008). These are transient and migratory features that generally lack a pronounced diurnal cycle (apart from local modifications). They are part of synoptic-scale eddies that feature a pronounced horizontal tilt in the mass and wind fields that accentuates the southwesterly (northwesterly) flow in the Northern (Southern) Hemisphere.

Perhaps the most commonly studied LLJs are those that maximize at night and form at least partly from the decoupling of the planetary boundary layer (PBL) after

* The National Center for Atmospheric Research is sponsored by the National Science Foundation.

Corresponding author address: Daran L. Rife, National Center for Atmospheric Research, P.O. Box 3000, Boulder, CO 80307-3000.
E-mail: drife@ucar.edu

DOI: 10.1175/2010JCLI3514.1

© 2010 American Meteorological Society

sunset. The so-called nocturnal LLJ (NLLJ) is a nearly ubiquitous feature. There are well-documented, spatially localized examples of NLLJs, some of which have a dramatic effect on transport near metropolitan areas. Studies by Mao and Talbot (2004) and Darby et al. (2006) show how a nocturnal jet occurring a few hundred meters above the ground can transport urban-generated chemicals well outside the urban area.

On larger, almost synoptic scales, NLLJs such as the low-level jet of the Great Plains of North America have been the subject of intensive study. Articles with substantial review material include S96 and Higgins et al. (1997). Recent articles that describe the relationship between the Great Plains NLLJ and rainfall are Tuttle and Davis (2006) and Carbone and Tuttle (2008). The basic findings are that the terminus or exit region of the NLLJ is frontogenetical. Lifting in this region destabilizes the lower troposphere by lifting parcels toward the level of free convection. Enhanced precipitation generally occurs near the exit region of the LLJ if there is weak baroclinity or if a moist jet encounters higher terrain.

Other relatively well-documented nocturnal jets include the South American NLLJ (Vera et al. 2006), which to first order appears as the mirror image of the Great Plains NLLJ and elicits a similar mesoscale convective response in the warm season (Salio et al. 2007). Other nocturnal NLLJs in South America have been noted, including a recurring jet in Brazil and jets near the north coast of South America associated with trade easterlies (Vernekar et al. 2003).

S96 also noted jets in other locations around the world, including Australia, South Africa, the Indian subcontinent, and Southeast Asia. However, compared to the poleward-flowing NLLJs in the Americas, these jets have been studied much less. The location of many NLLJs within the tropics and subtropics implies that they have an important influence on moisture transport and rainfall worldwide. NLLJs in arid regions can have a profound influence on the transport of aerosols such as dust (Todd et al. 2008) and pyrogenic products (Zunckel et al. 1996). Material lofted from the surface through the daytime turbulent boundary layer can be transported large distances at night. Koren et al. (2006) found that half of the mineral dust observed in the Amazon originated from the Bodélé depression in Chad. Dust is initially lofted by a diurnally varying, topographically enhanced LLJ within the broader-scale Harmattan, a dry northeasterly flow dominating the Sahara Desert in winter (Washington et al. 2006).

Low-level jets with substantial diurnal variability arise from essentially two mechanisms. The first, originally advanced by Blackadar (1957), depends on the decoupling and eventual recoupling of the lower troposphere to the surface through diurnally varying eddy viscosity that is driven by changes in solar heating. The second diurnal forcing mechanism for LLJs is the response to changes in horizontal baroclinity arising from spatial contrasts in insolation and from horizontal variations in the physiography. The solenoidal circulation that results from the transient horizontal temperature gradient yields a shallow, thermally direct flow from cool to warm air. This flow rotates in response to inertial forcing, yielding a jet that tends to flow parallel to the horizontal contrast in heating arising from either a land–sea boundary or a mountain–plain interface (e.g., Mo and Berbery 2004). Cessation of daytime heating may then result in an acceleration of the jet in a manner similar to that discussed earlier.

An important question is what allows an essentially local jet forcing mechanism to extend upscale to mesoscale and synoptic-scale corridors of strong wind that have a pronounced diurnal cycle. In some situations the synoptic-scale flow provided by migratory weather features can dramatically enhance or suppress the LLJ response. For instance, the development of a meridionally elongated lee trough to the east of the Rocky Mountains or Andes promotes poleward flow on the east side of the trough. Through boundary layer decoupling and recoupling, this poleward flow will execute a diurnal fluctuation in strength. However, such modulations of the NLLJs tend to be transient and are less important at the height of the warm season in midlatitudes and in all seasons in the tropics.

If migratory synoptic-scale features are relatively absent, there must be a broad length scale in the underlying physiography that leads to a NLLJ that is coherent over hundreds of kilometers. The Great Plains NLLJ is an excellent example whose structure builds on the downward-sloping surface from the Rockies to the Mississippi River (Byerle and Paegle 2003). The meridional quasi uniformity of the eastward-sloping terrain helps make the NLLJ coherent over a nearly 1000 km extent from north to south. This, along with the abundant moisture supply from the Gulf of Mexico to the south, ensures a systematic nocturnal transport of water vapor poleward over great distances. A similar argument applies to the South American NLLJ, where the Amazon is the immediate moisture source and the eastern slope of the north–south elongated Andes helps accentuate the nocturnal northerly flow. There are many physiographic features across the globe that have large length scales in at least one direction and therefore are candidates to host nocturnal jets that have a synoptic-scale influence. The goal of the present study is to objectively document the locations of NLLJs around the world and to examine their structure, both horizontal and vertical, as well as

TABLE 1. Model configuration used for the CFDDA global downscaled reanalysis.

Fully compressible nonhydrostatic dynamics
Twin polar stereographic grids, one centered over each pole and extending slightly beyond the equator; 40-km horizontal grid increment and 28 vertical levels, with approximately 12 levels within the lowest 1.5 km AGL; solutions joined at the equatorial interface using a Cressman-type horizontal interpolation function
Radiative upper-boundary condition that mitigates noise resulting from reflecting gravity waves
Time-dependent lateral boundary conditions, relaxed toward the NR2
Kain–Fritsch version 2 (Kain 2004) cumulus parameterization: month-long sensitivity tests showed this scheme produced the most realistic precipitation patterns and amounts compared to satellite-derived estimates
Reisner et al. (1998) microphysics, which predicts the mixing ratio of four hydrometeor species (cloud droplets, cloud ice, rain, and snow)
Computationally efficient Medium-Range Forecast (MRF) model PBL scheme (Hong and Pan 1996). A set of multiday sensitivity experiments showed that the spatial and temporal representation of NLLJs was not sensitive to choice of PBL scheme
Noah land surface model with four soil layers (Chen and Dudhia 2001a,b)
Cloud effects on radiative transfer (Dudhia 1989) for shortwave and Rapid Radiative Transfer Model (Mlawer et al. 1997) for longwave

their time evolution. The focus will be on jets that have an along-jet scale of several hundred kilometers and therefore exert a profound influence on the regional weather and climate. Representative cases of NLLJs in a variety of environments will be presented to better understand the mechanisms that produce these jets. Our goal is to emphasize the underlying commonalities of the jets.

Several tools are needed to accomplish our goal. The first, detailed in section 2, is a 21-yr global reanalysis performed with the fifth-generation Pennsylvania State University–National Center for Atmospheric Research (NCAR) Mesoscale Model (MM5) using a horizontal grid spacing of 40 km. Low-level jets with substantial diurnal variability have traditionally been difficult to study from a global perspective because of the lack of spatial and temporal resolution of available global reanalyses. A unique characteristic of the reanalysis used in this study is the availability of hourly output. This allows the full diurnal cycle to be analyzed. Furthermore, with a horizontal grid spacing of 40 km, many topographic features are better resolved than in widely used global datasets such as the National Centers for Environmental Prediction (NCEP)–NCAR reanalysis (NNRP; Todd et al. 2008). Thus, the diurnal variation of NLLJs, as well as the local forcing, is well represented in our analysis. This makes possible a detailed examination of the systematic onset and cessation of the jets, including time–height representations of the diurnal cycle.

The second tool is an index of NLLJ activity based upon the temporal variations in the wind's vertical profile, defined in local time (LT). This allows us to produce global maps in local time through which we can simultaneously view the objectively defined NLLJ index and thus have a quantitative analog of Fig. 1 in S96. This index is defined and applied in section 4, wherein the global occurrences of NLLJs are presented. Selected NLLJ regions are investigated in more detail in section 5 using representative cases from which characteristic meteorological patterns are presented. Conclusions appear in section 6. In a companion paper (Monaghan et al. 2010), we examine the linkages between NLLJs and precipitation maxima in regions where prominent recurring jets exist.

2. Global mesoscale reanalysis

As described in the introduction, NLLJs have been difficult to study from a global perspective because of the coarseness (space and time) of available global analyses. Thus, a primary objective of this paper is to describe and to verify a newly created global mesoscale reanalysis with hourly temporal resolution in three dimensions, permitting the diurnal cycle to be fully resolved. This analysis utilizes NCAR's Climate Four Dimensional Data Assimilation system (CFDDA; Hahmann et al. 2010). A summary of CFDDA and our technical approach is provided here, with additional details appearing in the appendix.

CFDDA is a dynamical downscaling system developed by NCAR to generate high-resolution climatographic analyses for any part of the world. At the heart of CFDDA is NCAR's Real Time Four Dimensional Data Assimilation system (RTFDDA; Liu et al. 2008), a mesoscale-model-based assimilation and forecasting system with versions based upon both the MM5 and its sequel, the Weather Research and Forecasting model (WRF; Skamarock et al. 2005). For the application described herein, we use the MM5-based version of CFDDA (MM5 version 3.6) to create global hourly analyses on a 40-km horizontal grid, with 28 vertical levels covering the period 1985–2005. The result is a database of (21 yr $\times$ 365 days $\times$ 24 h) three-dimensional analyses. Table 1

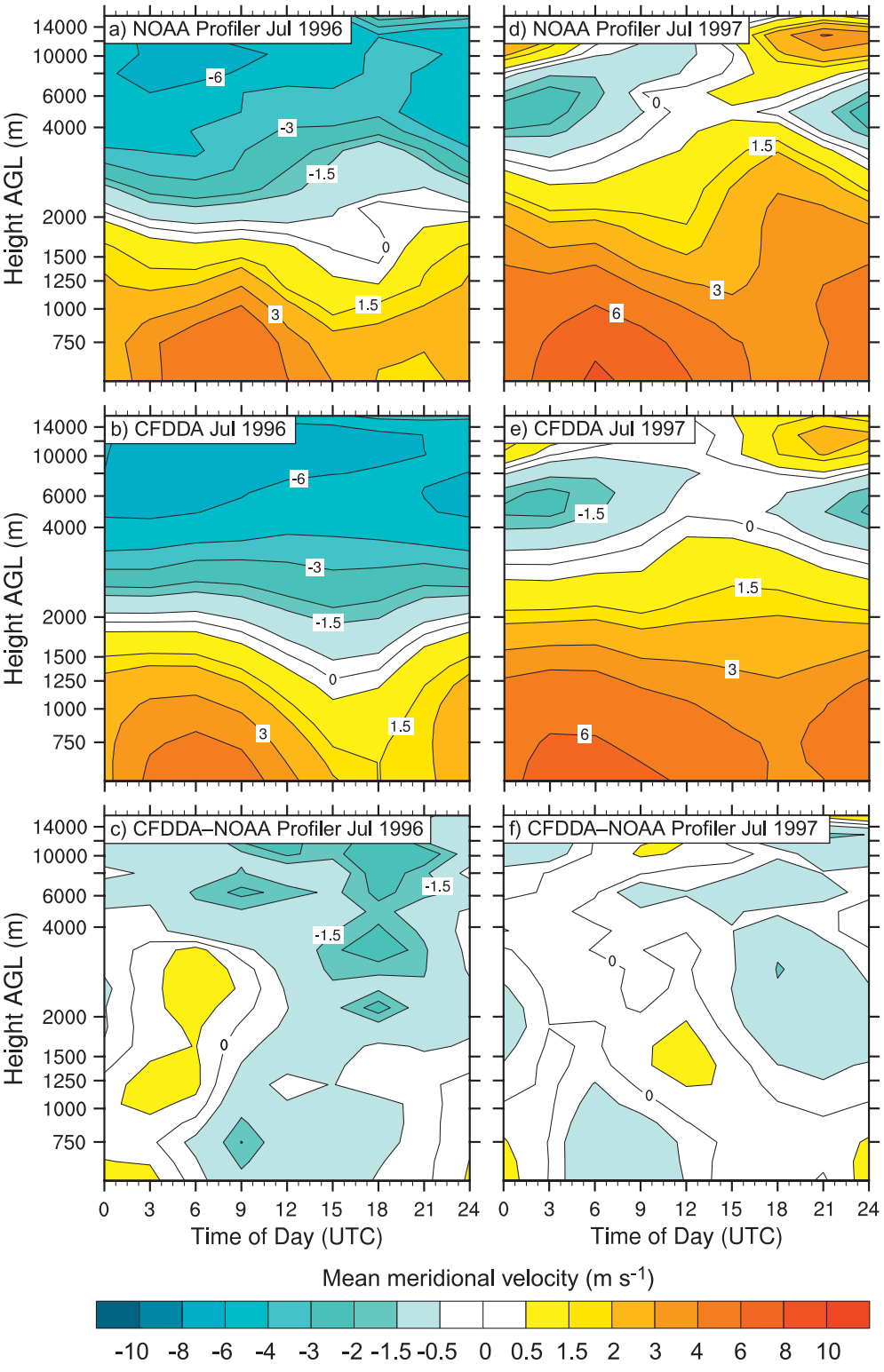

FIG. 1. Diurnally averaged meridional velocity for (a) NPN July 1996; (b) CFDDA July 1996; (c) CFDDA minus NPN July 1996; (d) NPN July 1997; (e) CFDDA July 1997; and (f) CFDDA minus NPN July 1997. The averages are a composite of five stations lying along the climatographic axis of the Great Plains NLLJ (97°W). Stations used for the composite are (from south to north), PRCO2, LMNO2, HBRK1, FBYN1, and NLGN1. The ordinate begins at 500 m AGL, corresponding to the lowest level of the profilers, and varies logarithmically with height. Note the color bar's uneven increments.

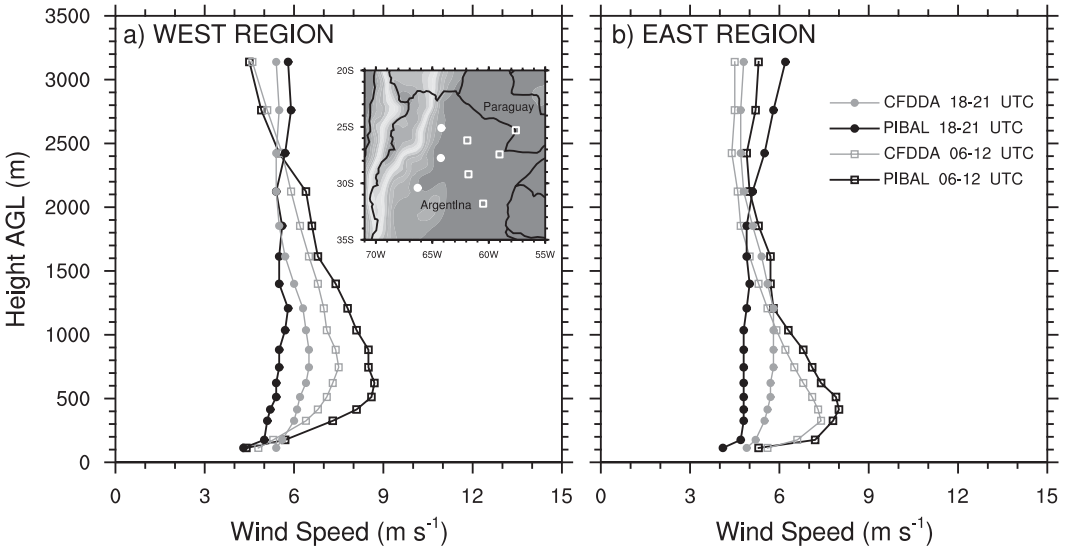

FIG. 2. Mean wind speed profiles (m s^{-1}) for PIBAL measurements and CFDDA for the SALLJEX region for January 2003. Composites for two regions, (a) west region and (b) east region, are created at both 1800–2100 and 0600–1200 UTC, corresponding to the approximate minimum and maximum times of the NLLJ. The inset shows the locations of the three stations used to calculate the west region composite (white circles) and the five stations used for the east region composite (white squares).

shows the physical process parameterizations chosen for maximum numerical stability and for producing the best representation of the mean structure and statistical behavior of the atmosphere within the boundary layer. Data used for initial and lateral boundary conditions are listed in the appendix.

Throughout the integrations, CFDDA continuously assimilates standard surface and upper-air observations using the Newtonian relaxation technique (Stauffer et al. 1991; Stauffer and Seaman 1994; Seaman et al. 1995). Observation data are obtained from the Advanced Data Processing datasets, available from the NCAR Research Data Archive. The global dataset contains both hourly and 6-hourly data reports collected by NCEP. The surface dataset includes mostly land reports, but a few ship observations also exist. The upper-air data are primarily standard rawinsonde measurements. The CFDDA solution is also nudged toward the driving NCEP–Department of Energy (DOE) Atmospheric Model Intercomparison Project (AMIP-II) reanalysis (NR2; Kanamitsu et al. 2002) at the upper levels to preserve the large-scale state in CFDDA, and to ensure mass conservation. A time-invariant vertical grid nudging zone is used, from the model top down to about 3.0 km AGL (above the average height of the PBL). The underlying principle is for the CFDDA large-scale solution to closely follow that of the NR2, while not impeding the ability of the assimilated observations and CFDDA to produce small-scale features, especially within the PBL.

3. Evaluation of the CFDDA global reanalysis

Before using the CFDDA mesoscale reanalysis for detailed, physically based study of NLLJs occurring in various environments, we first establish that CFDDA correctly replicates the mean characteristics of NLLJs, especially their diurnal and vertical structure. Unfortunately, only one of the NLLJ regions is well instrumented: the U.S. Great Plains NLLJ. Thus, our approach is to compare CFDDA's representation of the Great Plains NLLJ to a 12-yr subset of independent measurements from the National Oceanic and Atmospheric Administration Profiler Network (NPN). The NPN is located primarily within the central United States and has been operational since 1993. A total of 18 stations routinely measure hourly vertical profiles of wind from 500 m AGL to near the tropopause. These data were not assimilated by CFDDA or the driving NR2 analysis. We also evaluate the CFDDA-analyzed South American NLLJ using data from the South American Low Level Jet Experiment (SALLJEX; Vera et al. 2006), which took place from November 2002 to February 2003. To extend these results to other regions, we compare CFDDA to another well-known and thoroughly vetted global reanalysis: the European Centre for Medium-Range Weather Forecasts Interim Re-Analysis (ERA-Interim); Simmons et al. 2007; Uppala 2007). As with all data-assimilation-based reanalyses, CFDDA's representation of the PBL is expected to be superior where dense surface-based

TABLE 2. Mean characteristics for all NLLJs.

Site No.	Name	Location of jet core	Speed and direction at jet core (m s^{-1}/°)	Time of onset and cessation (LST)	Height of jet core (m AGL)
1	Great Plains	36.4°N, 100°W	14.6/200	18, 05	500
2	North Venezuela	10.4°N, 64.4°W	13.8/090	20, 09	600
3	Maracaibo	11.6°N, 70.4°W	14.6/090	15, 05	500
4	Syria	38°N, 36.8°E	11.6/330	22, 09	500
5	Iran	35.2°N, 57.2°E	15.9/060	21, 07	375
6	Tibet	30.4°N, 86.4°E	12.8/270	19, 06	400
7	Tarim Pendi	40.4°N, 83.2°E	9.3/040	21, 08	300
8	India	14.8°N, 76.8°E	18.9/270	19, 08	625
9	Southeast Asia	15.6°N, 102.4°E	14.3/260	21, 09	600
10	China	25.6°N, 113.6°E	11.7/190	22, 07	450
11	Venezuela*	6.8°N, 66.8°W	15.9/050	17, 09	500
12	Guyana*	4.0°N, 60.8°W	13.2/040	22, 08	450
13	Argentina*	34.4°S, 64.8°W	12.3/360	19, 03	400
14	Brazil*	29.2°S, 61.6°W	10.5/050	19, 03	350
15	Namibia*	16.0°S, 15.6°E	12.2/210	21, 05	300
16	Botswana*	23.6°S, 32.8°E	11.3/090	17, 01	350
17	Ethiopia*	12.8°N, 34.0°E	12.0/010	19, 08	400
18	Australia*	28.0°S, 124°E	12.3/060	20, 08	400

* Jet that occurs in austral summer.

measurement networks exist (e.g., the continental United States and Europe). In a companion paper (Monaghan et al. 2010), we evaluate CFDDA's ability to replicate the spatial and diurnal patterns of rainfall.

a. Diurnal and vertical structure of the Great Plains and South American NLLJs

1) GREAT PLAINS NLLJ

Because of the large amount of data processed for this study (12 yr of hourly NPN measurements at 18 stations and the corresponding hourly CFDDA analyses), the data and analyses are presented in reduced dimension format, where data are averaged in both space and time. Hourly measurements from five stations lying along the climatographic axis of the Great Plains LLJ (97°W) are composited to produce mean time–height representations of the NLLJ, using only those measurements that pass all NPN quality control tests (Miller et al. 1997), including the 6-step bird contamination detection algorithm described in van de Kamp et al. (1997) and Daniel et al. (1999). These stations are, from south to north, Purcell, Oklahoma (PRCO2); Lamont, Oklahoma (LMNO2); Hillsboro, Kansas (HBRK1); Fairbury, Nebraska (FBYN1); and Neligh, Nebraska (NLGN1). The same is done for CFDDA from grid points nearest to each of the five NPN sites. Again, the NPN data were not assimilated by CFDDA or the driving NR2 analysis, and thus provide an independent measure of how well CFDDA simulates the diurnal LLJ variability in this region. We note that although the NPN provides a good overall depiction of the NLLJ within Great Plains region, because its first measurement level is at 500 m AGL, it tends to underrepresent both the strength and frequency of occurrence of the NLLJ (Mitchell et al. 1995; Daniel et al. 1999). Figure 1 presents the results for July 1996 and July 1997, during a period where the weather and climate over North America was strongly influenced by the ENSO cycle. Overall, CFDDA's representation of the vertical structure and timing of the NLLJ is excellent, with the mean jet forming near 0300 UTC and reaching its maximum strength at 0600 UTC. For both years, the CFDDA jet core is slightly weaker than observed, and the vertical extent of the jet core is modestly underrepresented by CFDDA, resulting in an overall negative bias of approximately 0.5–1.5 m s^{-1} at nearly all levels during the day, and a positive bias of about 0.5–1.0 m s^{-1} for most levels during the night (Figs. 1c,f). The errors lie within the NPN's envelope of observational uncertainty, which is estimated to be 0.5–1.0 m s^{-1}, with a standard deviation of 2.5–4 m s^{-1} (Weber and Wuertz 1990; Martner et al. 1993). These results are broadly consistent with the NLLJs observed for other years during the warm season.

A noteworthy feature appearing in both the NPN data and CFDDA is a diurnal reversal of the wind at 4–6 km AGL and another at about 12 km AGL, directly above the NLLJ core. These features appear repeatedly in other years and are most prevalent during the warm season. Such upper-level wind field oscillations within the Great Plains NLLJ region have been reported by Hering and Borden (1962), Helfand and Schubert (1995), Higgins et al. (1997), and Jiang et al. (2007). Helfand and Schubert (1995) ascribe the diurnal wind reversal at

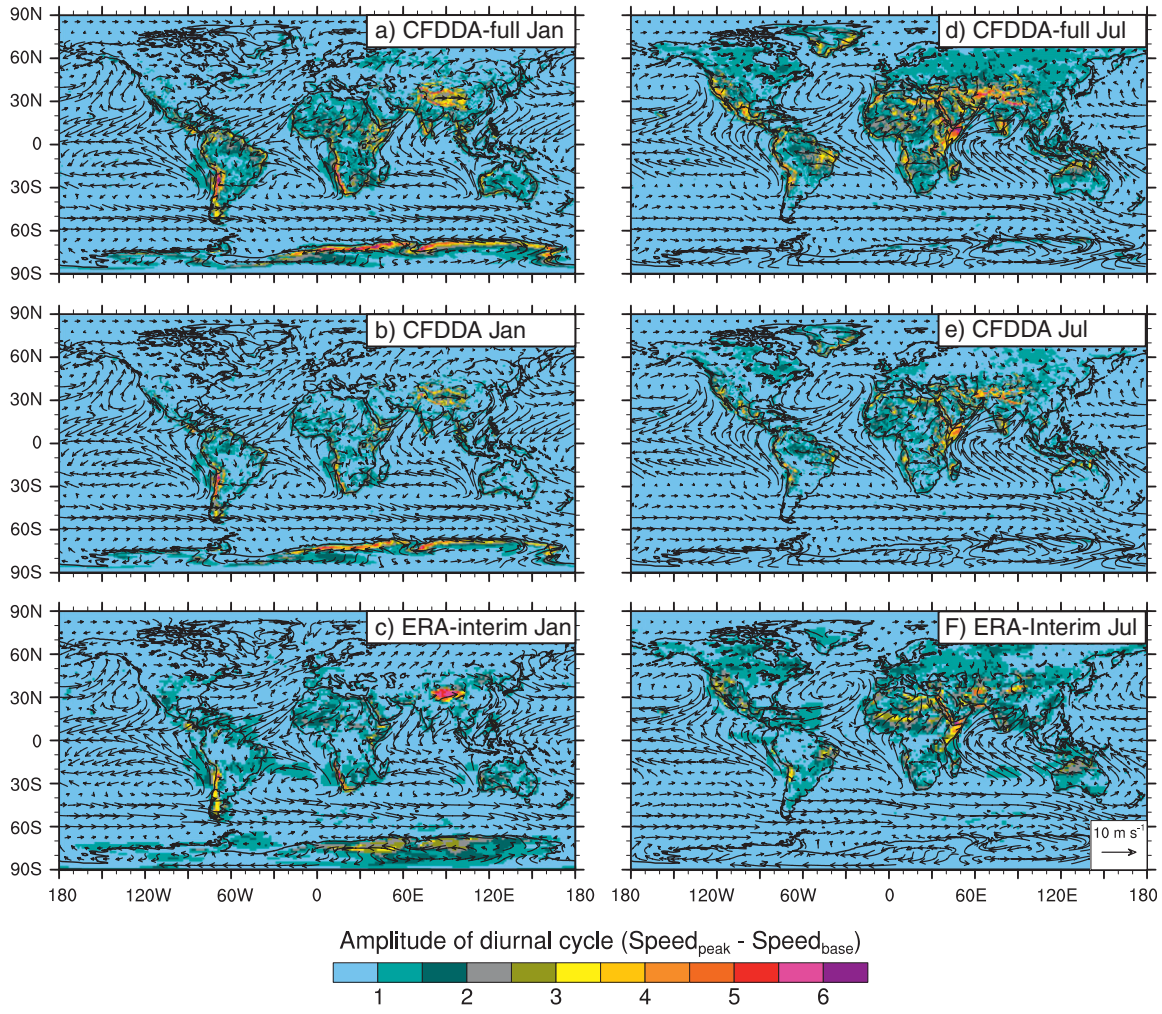

FIG. 3. Amplitude of the mean diurnal cycle of near-surface winds for 2001–05 for (left) January and (right) July, where the amplitude is expressed as the difference between the mean wind speed at the peak and base of the diurnal cycle at each grid point (shaded; units of m s^{-1}). The mean near-surface winds (arrows) at the peak of the diurnal cycle are also shown. The diurnal cycle for (b),(e) CFDDA and (c),(f) ERA-Interim calculated for the 6-hourly output times available in the ERA-Interim dataset (i.e., 0000, 0600, 1200, and 1800 UTC); (a),(d) CFDDA's mean diurnal cycle calculated from its full *hourly* output dataset (labeled "CFDDA-full"). CFDDA wind vectors are plotted at approximately every 20th grid point, and ERA-Interim wind vectors are plotted at approximately every 5th grid point.

4–6 km AGL to thermal uplift, which they call a "thermal chimney," where warmer air from below is "ventilated" aloft during the day, inducing convergence at low levels and divergence in the middle levels, with the reverse circulation forming at night. However, this phenomenon may simply be a reflection of the return branch of the broad mountain–plain circulation (e.g., Whiteman 2000), which flows eastward, but inertial forcing progressively turns it to the right such that upon arriving over the NLLJ core, the flow is directed southward along the jet axis.

Another aspect worth highlighting is the strong interannual variation in the mean NLLJ structure. Most notable is the persistent northerly flow above about 2 km AGL over the five stations during July 1996, with evidence that the aforementioned diurnal wind reversal aloft is apparently overwhelmed by a dominant large-scale northerly flow. CFDDA correctly depicts this year-to-year variability.

2) SOUTH AMERICAN NLLJ

Another relatively well-documented nocturnal jet is the South American NLLJ, which is the approximate mirror image of the Great Plains NLLJ (Nogués-Paegle and Mo 1997), and gives rise to a similar mesoscale convective response in the warm season (Salio et al. 2007). Though it is less well instrumented than the Great Plains NLLJ, we use data from the SALLJEX field program,

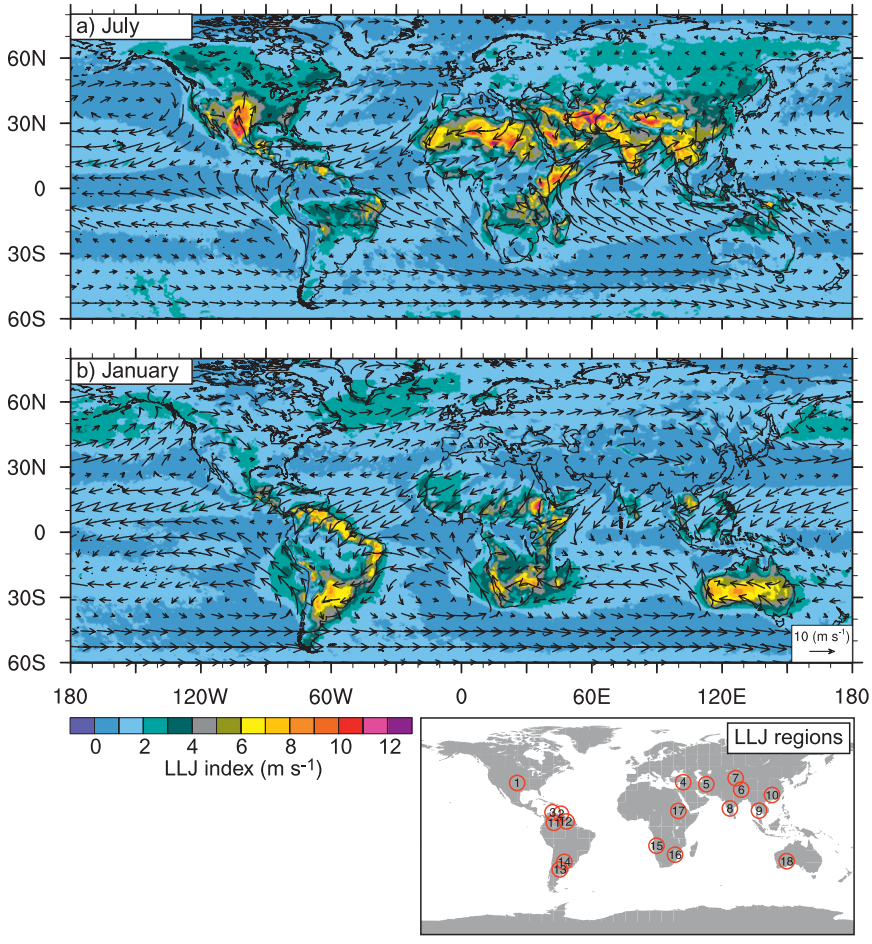

FIG. 4. Mean NLLJ index (shaded) and 500-m AGL winds (arrows) at local midnight for 1985–2005 for (a) July and (b) January calculated from the CFDDA hourly analyses. The inset shows the locations of NLLJs analyzed for this study, whose characteristics are summarized in Table 2. Vector winds are plotted at approximately every 20th grid point.

which took place from November 2002 through February 2003 (Vera et al. 2006). An enhanced network of pilot balloon (PIBAL) measurements was available throughout the study period, primarily at 0900, 1200, 1800, and 2100 UTC. As with the NPN data, none of the PIBALs was assimilated by CFDDA or the driving NR2 analysis. Figure 2 shows the mean wind speed profiles for CFDDA and the PIBALs over the SALLJEX region for January 2003. Month-long composites for two regions, called ''west region'' and ''east region'', are created at both 1800–2100 and 0600–1200 UTC, corresponding to the approximate minimum and maximum times of the NLLJ. These two regions host NLLJ maxima and are labeled as *Argentina* and *Brazil* in Table 2. The locations of the three stations used to calculate the west region composite, and the five stations used for the east region composite are shown in Fig. 2.

Overall, CFDDA's representation of the vertical structure and timing of the NLLJ is reasonable, with the jet maxima forming at 0600–1200 UTC and reaching its maximum strength at about 500 m AGL for both regions. For both locations, the CFDDA jet core is slightly weaker than observed, and the vertical position of the jet core is somewhat higher (lower) than observed for the west (east) region. In both cases, CFDDA overestimates the winds speeds during the afternoon by about 1 m s^{-1}. Visual inspection of the CFDDA analyses shows that the analyzed jet core over the west region was placed farther south than observed (not shown).

b. Global diurnal cycle of near-surface winds

To extend these results to other regions, we now compare CFDDA's representation of the global diurnal cycle of near-surface winds to that in ERA-Interim. Figure 3 shows the amplitude of the mean diurnal cycle of winds for 2001–05 for January and July, where the amplitude is expressed as the difference between the

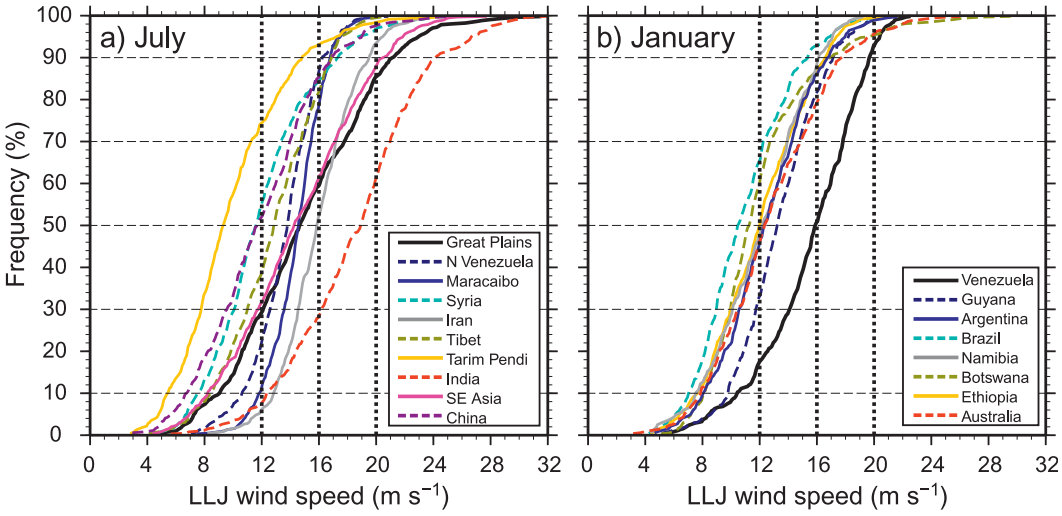

FIG. 5. Empirical cumulative frequency distributions of LLJ wind speeds for the 18 locations identified in Fig. 4 for 1985–2005 for (a) July and (b) January. The wind speed is defined at or near the climatographic peak time and height of each jet (i.e., local midnight at 500 m AGL). Wind speed distributions for each location are conditioned upon the LLJ index being greater than zero. The number of nonzero NLLJ index values for each region is shown in Fig. 6. The thick, dotted black lines mark the three LLJ wind speed (ws) classifications defined by Bonner (1968): ws $\geq$ 12 m s^{-1}; ws $\geq$ 16 m s^{-1}; and ws $\geq$ 20 m s^{-1}.

mean wind speed at the peak and base of the diurnal cycle at each grid point. The mean near-surface winds at the peak of the diurnal cycle are also shown. The strongest diurnal variability occurs along the coastlines and elevated terrain during the warm season in both hemispheres, reflecting the dominance of thermally driven winds at these locations. The diurnal magnitudes of CFDDA and ERA-Interim are comparable; however, because the peak and base of the diurnal cycle at many locations are offset from the 6-hourly output times available in the ERA-Interim, there is a significant underrepresentation of the diurnal change, as shown by CFDDA-full in the top panels of Fig. 3. There is an especially strong diurnal change exhibited by the ERA-Interim over the Tibetan Plateau in January. Surface observations on the eastern half of the plateau (e.g., Tuotuohe, China, at 34.22°N, 92.43°E) suggest that the 5–6 m s^{-1} diurnal variation exhibited by the ERA-Interim is reasonable. CFDDA's diurnal cycle over the plateau in January is somewhat muted compared to the observations and ERA-Interim, but the two reanalyses have a comparable diurnal change in July.

The global wind patterns are also evident in Fig. 3, including the tropical and subtropical trade winds during both summer and winter. The semipermanent Bermuda–Azores high and its counterpart, the Pacific high, are also well represented by CFDDA in July. Flows associated with the persistent Icelandic and Aleutian lows are readily seen in January. Finally, the winter and summer Asian monsoon are also well represented by CFDDA. In summary, these results clearly demonstrate that CFDDA is capable of representing the diurnal evolution of the mean structure of winds within the PBL and therefore justify its use for detailed physical studies of diurnally varying LLJs.

4. Mapping the locations of recurring NLLJs

a. *Concept*

Although S96 prepared a hand-drawn map of LLJ locations, we seek a quantitative cartographic technique for plotting LLJs that can be applied to any gridded dataset with sufficient temporal and spatial resolution. To this end, we develop an index of NLLJ activity based upon the vertical structure of the wind's temporal variation, defined in local time. This allows us to produce the first objective maps of recurring NLLJs around the world, where the jets can be simultaneously viewed at or near their peak time. Because NLLJs are primarily a warm-season phenomenon, our focus is on months at the height of the summer season in each hemisphere (i.e., January and July). However, the technique described here can readily be applied to other months to explore the seasonal variability of the jets.

b. *Index of NLLJ activity*

We start with the 21-yr collection of hourly output from CFDDA for January and July. Each hourly output

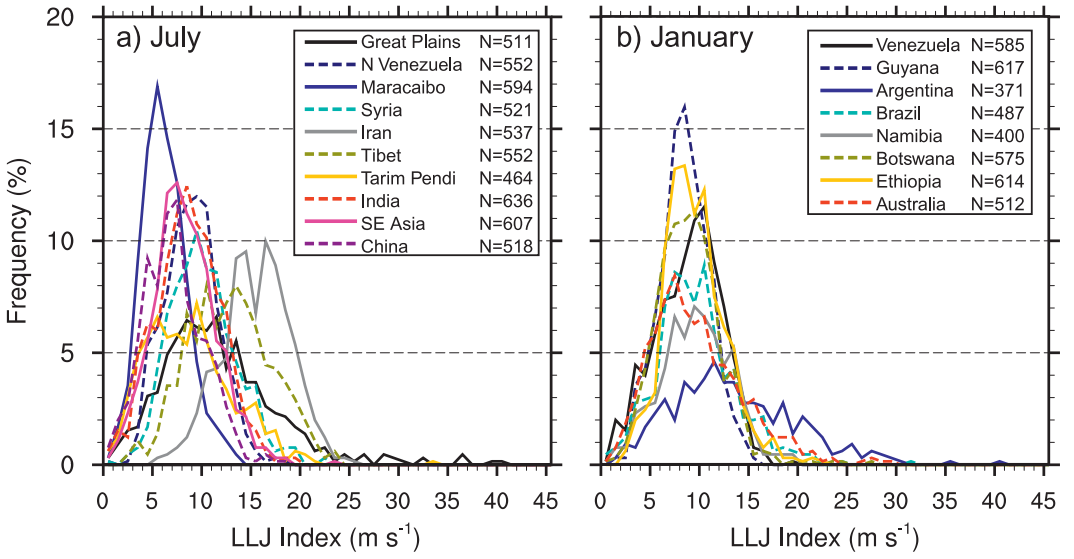

FIG. 6. Distributions of NLLJ indices for the 18 locations identified in Fig. 4 for 1985–2005 for (a) July and (b) January. The number of nonzero NLLJ index values for each region is shown in the legend. There are a total possible of 651 days (31 days × 21 yr) for either July or January.

is assigned the local time within each 15° longitudinal strip on the globe. For example, the 0600 UTC output over the Great Plains region, centered at 100°W, would be assigned a time of 0000 LT. The winds at each grid point are then classified as being associated with an NLLJ according to two criteria, and both must be satisfied simultaneously. The first requires the winds at 500 m AGL (near jet level) to be stronger at local midnight than at local noon. The second requires the wind speed at the jet's core (500 m AGL) to be stronger than that aloft (4 km AGL), similar to the criterion of Whiteman et al. (1997). The NLLJ index (m s^{-1}) is therefore both a function of the difference between winds near the surface and those aloft, and the diurnal variation of the winds. Given these rules, the NLLJ index *NLLJ* is defined at each grid point according to

$$NLLJ = \lambda\varphi\sqrt{[(u_{00}^{L1} - u_{00}^{L2}) - (u_{12}^{L1} - u_{12}^{L2})]^2 + [(v_{00}^{L1} - v_{00}^{L2}) - (v_{12}^{L1} - v_{12}^{L2})]^2}, \quad (1)$$

where u and v are the zonal and meridional wind components, respectively. The superscripts $L1$ and $L2$ denote winds at 500 and 4000 m AGL, respectively, and represent winds within the jet core and those above the core. As shown later, the various jets are at their maximum at about 500 m AGL, consistent with the 300–600-m mean height range for the Great Plains NLLJ reported by Whiteman et al. (1997) and others. The subscripts 00 and 12 denote *local* midnight and *local* noon. Because the term under the square root is positive, two additional terms are needed to account for the algebraic signs of the vertical and temporal changes in the wind. The first, lambda (λ), is a binary multiplier that requires the difference between the 500 m AGL wind speed (ws) at local midnight and local noon to be positive,

$$\lambda = \begin{cases} 0, & \text{ws}_{00}^{L1} \le \text{ws}_{12}^{L1} \\ 1, & \text{ws}_{00}^{L1} > \text{ws}_{12}^{L1} \end{cases}. \quad (2)$$

The second, phi (φ), is also a binary multiplier that requires the 500 m AGL wind speed at local midnight to be greater than that at 4000 m AGL at the same time. This ensures that the winds conform to a jet-like profile,

$$\varphi = \begin{cases} 0, & \text{ws}_{00}^{L1} \le \text{ws}_{00}^{L2} \\ 1, & \text{ws}_{00}^{L1} > \text{ws}_{00}^{L2} \end{cases}. \quad (3)$$

We experimented with several variants of (1) and found the present version to be very effective at filtering out synoptically driven wind systems that would otherwise contaminate the NLLJ event database. The result is a database of daily NLLJ index values for the entire 21-yr period, which is used to form composite global maps of NLLJ activity that highlight not only the locations for recurring jets, but also their mean strength, horizontal extent, and geographic orientation.

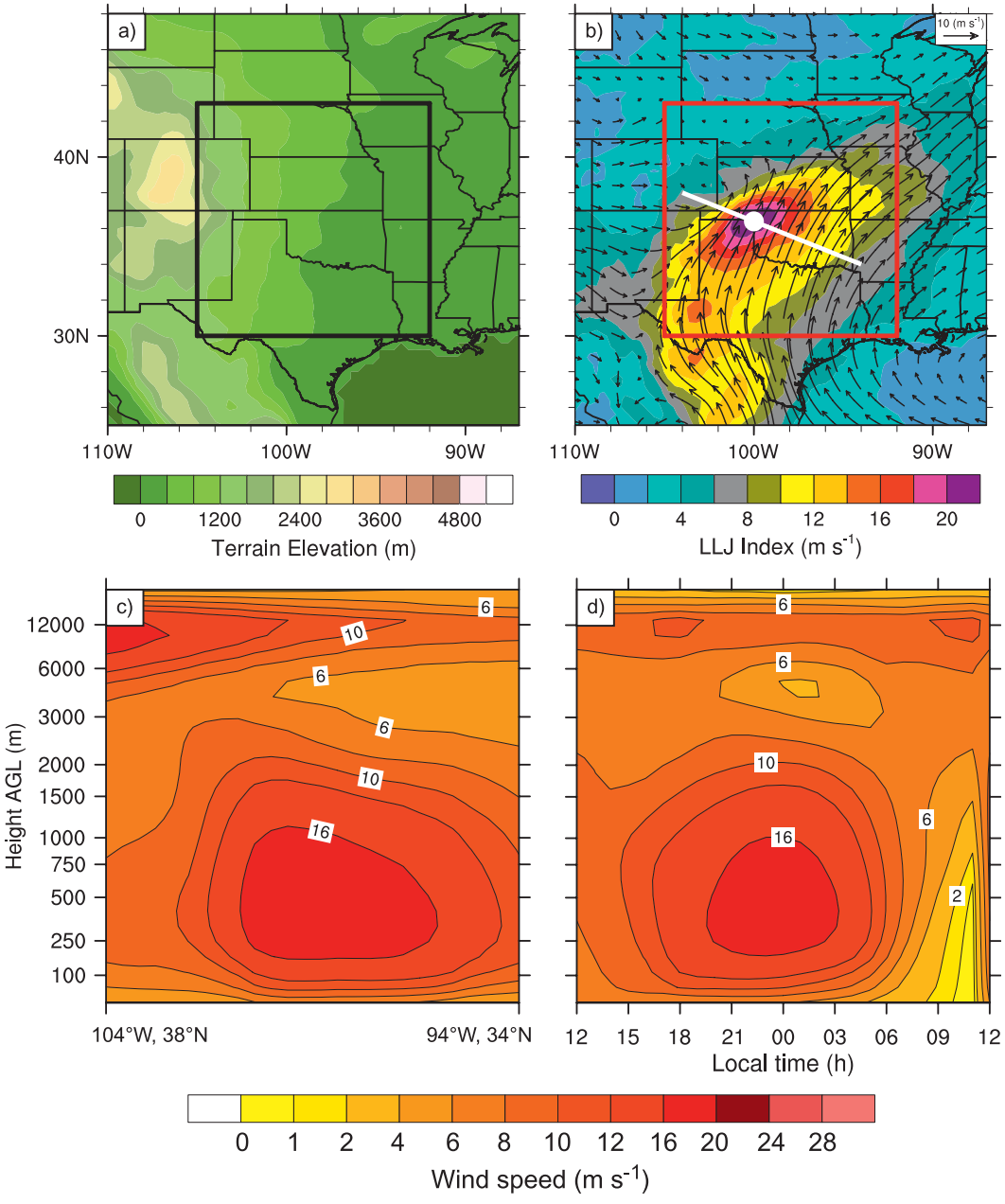

FIG. 7. Composite characteristics for strong (≥90th percentile) NLLJ events for the Great Plains region (site 1 in Fig. 4b) for July 1985–2005. (a) Terrain elevation within the region (meters MSL) and (b) mean NLLJ index (shaded) and 500-m AGL winds (arrows). Vector winds are shown at local midnight at each point and are plotted at approximately every third grid point. Thick white line denotes the location of the cross section shown in panel (c), and the white circle denotes the point at or near the jet core, and marks the location of the time–height plot shown in panel (d). (c) Cross section of the mean wind speed along the white line in (b). (d) Mean time–height of wind speed within the jet core, denoted by the white circle in (b). Thick black and red lines in (a) and (b) show the visually defined box centered on the 21-yr average NLLJ core that is used to calculate the mean characteristics of NLLJs presented in Table 2.

c. *Global NLLJ maps*

Figure 4 shows the 21-yr mean daily NLLJ index maps January and July. The mean 500-m-AGL wind vectors at 0000 LT are also shown (the approximate height and time of the jet maxima) to highlight the horizontal structure of the jets. Information poleward of 80°N and 60°S is omitted, because the land ice, sea ice, and ocean surfaces

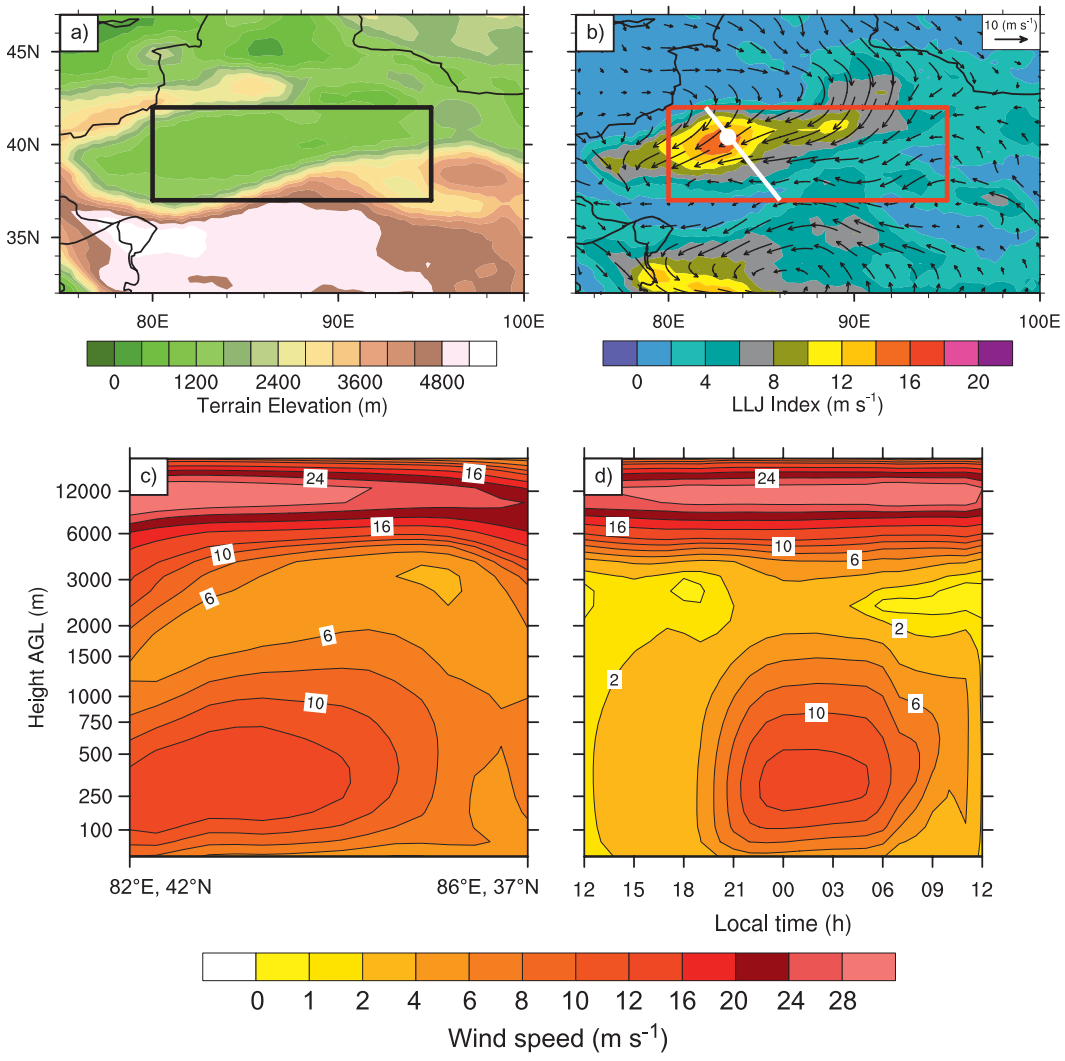

FIG. 8. As in Fig. 7, but for the Tarim Pendi NLLJ events for July 1985–2005 (site 7 in Fig. 4b).

in the polar regions greatly dampen the diurnal cycle at the peak of the warm season and thus no NLLJs occur within these latitudes. The inset shows the locations of the numbered NLLJs analyzed herein, whose characteristics are summarized in Table 2; four of these are subject to detailed study in section 5. The jets were chosen based on their known or suspected link to heavy nocturnal precipitation (Monaghan et al. 2010), with a special emphasis on the newly identified jets. All the known NLLJs in Fig. 1 of S96 appear clearly in our objective maps, including the Great Plains NLLJ (site 1); the South American NLLJ (sites 13 and 14); the jets over Maracaibo (site 3) and north Venezuela (site 2), which are part of the larger-scale Caribbean LLJ; the jet over southeast China (site 10); the southerly flowing NLLJ over Baja California (not numbered); and the coast-following western Australia NLLJ (site 18). Although most of the NLLJ maxima are evident over land areas during summer, there are some notable exceptions. For example, a strong NLLJ forms in Ethiopia (site 17) during boreal winter, even though the jet core forms near 10°N. In addition, there are weak NLLJs over the Brazilian Highlands in South American and East Africa's Great Rift Valley (not numbered) during austral winter, neither of which has been previously documented.

These maps show several newly identified areas of intense NLLJ activity, most lying in the Northern Hemisphere, and numbered in the inset of Fig. 4 and Table 2. These include Syria (site 4), Iran (site 5), Tarim Pendi (site 7), Tibet (site 6), Ethiopia (site 17), Venezuela (site 11), Guyana (site 12), Maracaibo (site 3), Namibia (site 15), and Botswana (site 16). Many of these NLLJs are associated with large moisture fluxes, whereas others are associated with the lofting and transport of dust. An especially

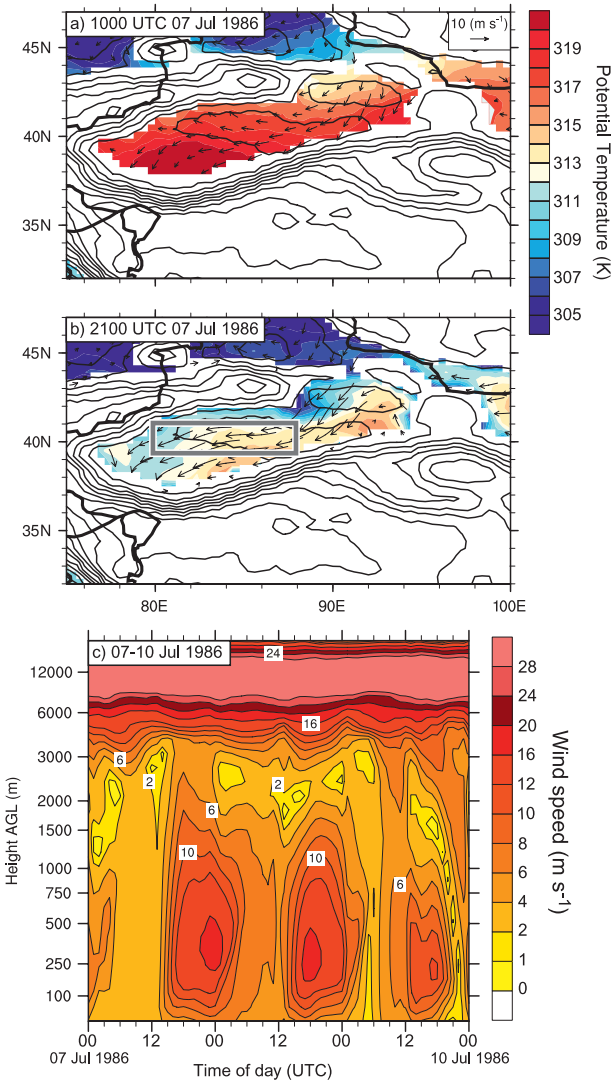

FIG. 9. Characteristics of the Tarim Pendi NLLJ for a multiday episode during 7–10 Jul 1986. Potential temperature (shaded) and winds (arrows) at 850 hPa for (a) 1000 and (b) 2100 UTC 7 Jul 1986. Thin black lines show terrain elevation in increments of 500 m. Vector winds are plotted at approximately every third grid point. (c) Time–height plot of mean wind speed within the jet core, whose position is denoted by the white circle in Fig. 8b. Thick gray lines in (b) show the visually defined box that bounds the region of the peak nocturnal acceleration and is used to calculate the horizontal momentum budget presented in Fig. 10.

large feature not numbered in Fig. 4 is the NLLJ that stretches westward across Egypt to Libya to Algeria and onward to western Sahara, which may play a large role in regional dust transport. Western Sahara dust emissions are at their peak in June and July (Engelstaedter and Washington 2007). This jet appears to conform strongly to the thermal wind relationship, with relatively warm air lying to the north and west over the Mediterranean Sea and Atlantic Ocean, and air that undergoes intense radiative cooling over the Sahara Desert to the south. A strong, recurring Saharan NLLJ also appears in the ERA-Interim at 850 hPa for July 2000–05 (not shown), further suggesting this feature's significance.

Table 2 lists the mean characteristics for each of the 18 jets studied herein. The maxima for the various jets occur between 300–600 m AGL with jet core winds generally greater than 10 m s^{-1}. The weakest jet is found over Tarim Pendi (9.3 m s^{-1}), whereas the strongest is found over India (18.9 m s^{-1}). The orientation of NLLJs includes all four primary directions (north, south, east, and west), with the mean direction in each region depending strongly on the geographic orientation of the adjacent physiography and the underlying horizontal heat contrasts. The onset time of the NLLJs is typically late afternoon; however, the time of cessation is more variable, often occurring well before sunrise. Figure 5 shows the frequency distributions of NLLJ wind speeds at each location in Fig. 4. The wind speed is defined at or near the climatographic peak time and height of the jets (i.e., local midnight at 500 m AGL; the geographic location for each jet core is listed in Table 2). The Bonner (1968) LLJ wind speed classifications are marked on the figure to help connect our results to previous studies. The distributions for the jets are strikingly similar, with most of the NLLJs having wind speeds at or below 16 m s^{-1} (Bonner's category 2), and wind speeds $\geq$ 20 m s^{-1} rarely occur. The notable exception to this is the India NLLJ (red curve, July), whose wind speeds exceed 20 m s^{-1} about 40% of the time. Interestingly, all but one of the strongest NLLJs lie within the Northern Hemisphere (Great Plains, India, Iran, and Southeast Asia), and three of these originate at or near the ocean. The Northern Hemisphere continental expanses tend to produce stronger large-scale land–sea temperature contrasts compared to the Southern Hemisphere. The stronger temperature gradients that result drive more intense NLLJ accelerations. Another noteworthy characteristic is that the latitude for most jets is within 30° of the equator. Equatorward of 30°, the diurnal land–sea variation produces inertia gravity waves that can propagate far from their origin (Rotunno 1983). Poleward of 30°, the atmospheric response is localized (e.g., the familiar sea breeze).

Figure 6 shows the distributions of NLLJ indices at each of the locations identified in Fig. 4 for 1985–2005 to assess the jets' typical diurnal variations. Average NLLJ index values are computed within a visually defined box centered on the NLLJ's climatographical mean core for each region (see, e.g., the black boxes in Figs. 7a, 8a, 11a, 14a) for the season having the strongest NLLJ (January or July) in a given location. Box sizes depend on the horizontal scale and geographic

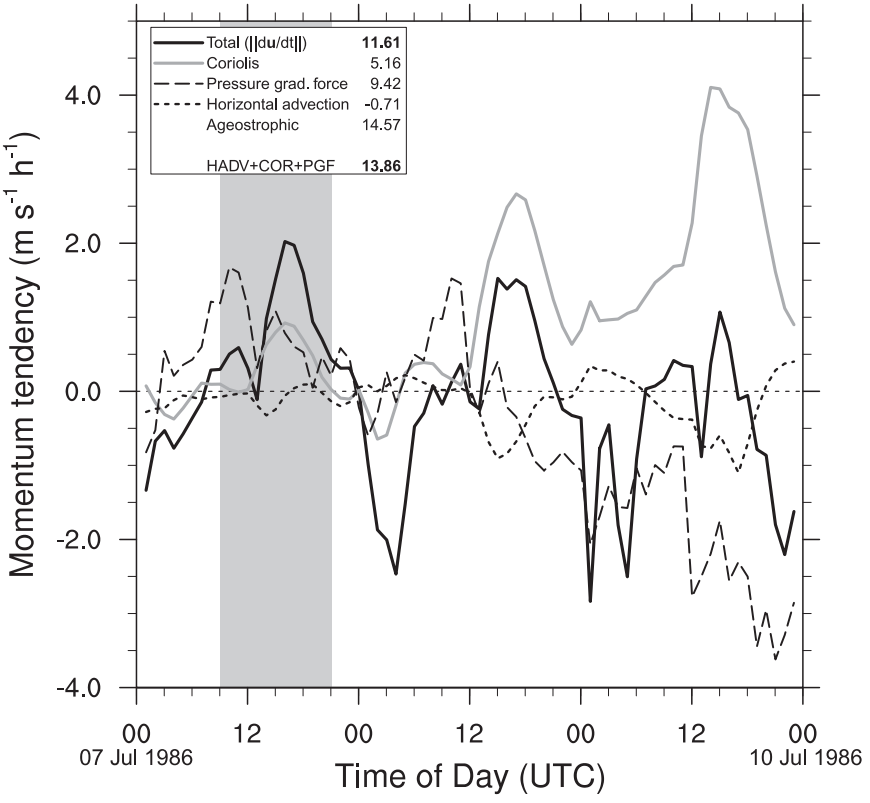

FIG. 10. Time series of the individual terms in the horizontal momentum budget at 850 hPa, for the Tarim Pendi NLLJ for 7–10 Jul 1986, averaged over the acceleration region denoted by the gray lines in Fig. 9b. The vertical gray bar bounds the times of the plan view plots in Figs. 9a,b, and marks the interval over which the integrated acceleration is calculated for the various momentum terms, whose values are reported in the top-left corner of the plot. The ageostrophic term is expressed as sum of the accelerations due to the PGF and the Coriolis force.

orientation of each jet, but they typically encompass a 10°–15° latitudinal extent and a 15° longitudinal extent. The frequency distributions of most jets are remarkably similar with peaks around 10 m s^{-1}. Two jets have a particularly strong change: Iran and Tibet. The LLJ over Iran undergoes a nearly 17 m s^{-1} variation (site 5; gray curve in Fig. 6a), whereas the Tibet LLJ typically experiences a 14 m s^{-1} daily change (site 6; dashed yellow curve in Fig. 6a). The frequency distributions for the Great Plains and Argentina jets have relatively long tails. This may reflect the influence of synoptic-scale variations. The Maracaibo LLJ exhibits a much weaker frequency maximum at 5 m s^{-1} (site 3; blue curve in Fig. 6a) and rarely exceeds a diurnal change of about 12 m s^{-1}.

5. Detailed study of select NLLJs

In this section, we examine the basic mechanisms producing the diurnally varying low-level jets identified in disparate locations around the globe. For brevity, only four jets are selected; for these, a consistent but modest amount of material will be presented to illustrate the processes involved in producing each jet. This will include representative, multiday case studies.

The first example is the well-known Great Plains NLLJ of North America. The diurnal flow during the day is dominated by near-surface southeasterly winds that occur in response to the extensive heating of the high terrain near 105°W (Fig. 7a). Sometimes this is aided by a synoptic-scale surface low-pressure area that forms on the east side of the central or southern Rocky Mountains. As shown by Blackadar (1957), much of the behavior of the jet is captured by simple inertial motion that is assumed to initiate as mixing ceases during the evening when the boundary layer decouples from the atmosphere above. The simple idea works surprisingly well considering that it assumes no subsequent mixing or time variation of the pressure gradient, neither of which is an accurate assumption (Hoecker 1965; Holton 1967). Holton (1967) showed that the pressure-gradient force undergoes a diurnal variation in response to the daytime

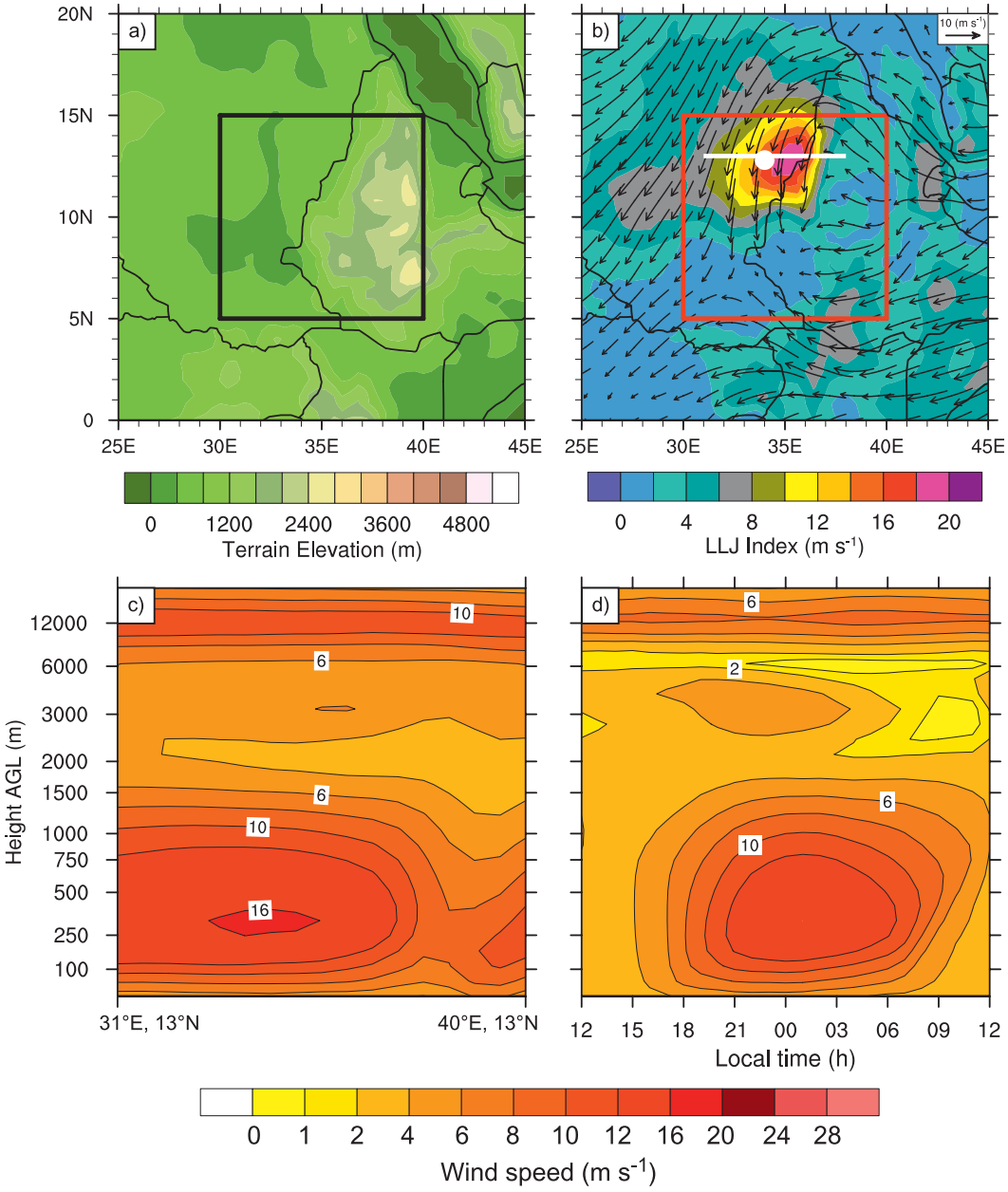

FIG. 11. As in Fig. 7, but for the Ethiopia NLLJ events for January 1985–2005 (site 17 in Fig. 4b).

elevated heating over terrain and nonuniform nocturnal cooling that tends to reinforce the inertial oscillation.

Bonner (1968) showed the climatography of low-level jets across the United States. Clearly a warm-season phenomenon, the maximum frequency occurs over the southern plains. Note, however, from Fig. 4 that there is a secondary southwesterly jet maximum along the Atlantic coast that also appears in Bonner's 2-yr climatography. The Great Plains jet appears as southerly flow in the early evening, but by midnight it rotates to a southwesterly direction (Fig. 7b) and intensifies (Fig. 7d). The jet in this region is deep compared with other NLLJs we will show (note the skewed vertical scale used in Figs. 7c,d).

The second example is the Tarim Pendi NLLJ (site 7 in Fig. 4b). This jet occurs somewhat less often and with smaller amplitude than the Great Plains jet of North America (Fig. 6). It is a warm-season phenomenon, occurring near 40°N. Examination of time series of soundings from Kuqa (not shown), located on the north side of the Tarim Basin over which the jet occurs, suggests that the jet is highly episodic. Jet occurrence follows the

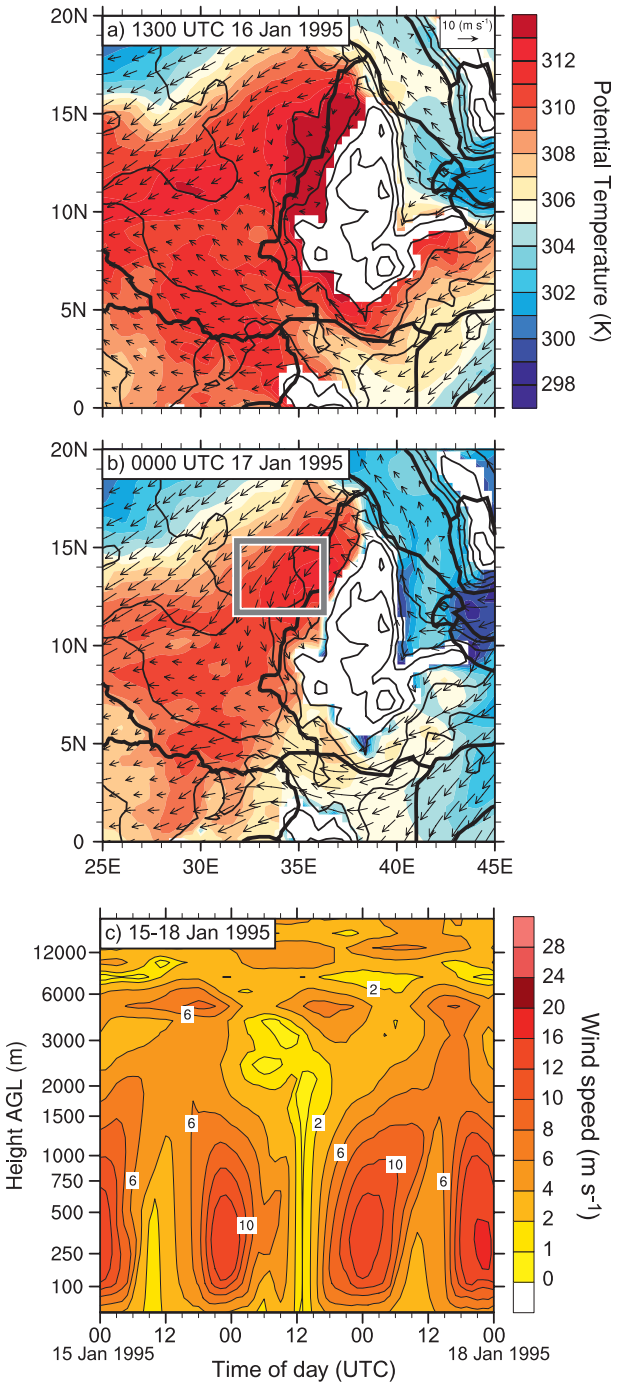

FIG. 12. As in Fig. 9, but for the Ethiopian NLLJ for a multiday episode during 15–18 January 1995. Time–height plot is for the jet core whose position is denoted by the white circle in Fig. 11b. Vector winds are plotted at approximately every second grid point.

passage of cold fronts around the Tian Shan mountains to the north (Fig. 8a), such that the cold air enters the region from the east and northeast (Figs. 8b, 9a,b). The jet maximizes at a height of about 300 m AGL, although there is evidence in this case that the jet becomes shallower over the terrain slope. The time of maximum intensity is between local midnight and 0300 LT,[1] and the jet dissipates around sunrise. Strong westerlies are apparent in the upper troposphere, and the region is typically on the anticyclonic shear side of the upper-tropospheric jet during these events.

We quantify the development of the nocturnal jet using a momentum budget similar to that used by Doyle and Warner (1993). In the present case, we do not have access to the full dissipation terms, because they were not archived in the reanalysis. Therefore, the tendencies of momentum are compared to forcing by the pressure gradient (PGF), Coriolis, and advection terms. The budget represents an average over a rectangular box that bounds the region of the nocturnal acceleration. Note that even though we neglect the additional dissipation terms, their contribution is probably secondary when integrated over the development time of the jets. There is typically a slight excess of momentum forcing, which is about 25% for the Namibia jet and 5%–6% for the Ethiopia and Tarim Pendi jets. At each point within the box, the terms in the vector momentum equation are projected onto the time average of the vector wind acceleration during the roughly 12-h period that defines the spinup of the jet. The projected vectors are then averaged spatially over the box to produce a time series of hourly acceleration contributions. The budget is computed on either the 850- or 900-hPa pressure surface, selected as the level that lies closest to the level of the maximum vector wind change. Positive values of forcing terms indicate a tendency to strengthen the jet, and negative values indicate a tendency to weaken the jet.

In the Tarim Pendi example, the period chosen is 0900–2100 UTC 7 July 1986. Overall, the Tarim Pendi jet has the character of a barrier jet along the Tian Shan mountains with a strong PGF directed southward balanced nearly by a Coriolis force directed northward (not shown). The imbalance between these two forces becomes significant over the northern Tarim Basin, resulting in a strong acceleration along the mountains. Shown in Fig. 10 are time series of the hourly momentum tendency contributions as well as the simulated momentum tendency. The direction onto which the forcing terms are projected is toward the west-southwest. In general, all terms exhibit considerable diurnal oscillation, but with clear trends

[1] These times are based on longitude and the position of the sun, not on the actual local time. Because China contains only one time zone, sunrise and sunset in the Tarim Pendi region occur 2–3 h later than we might expect for this latitude. Hence, local midnight by our definition would be 0200–0300 in actual local time.

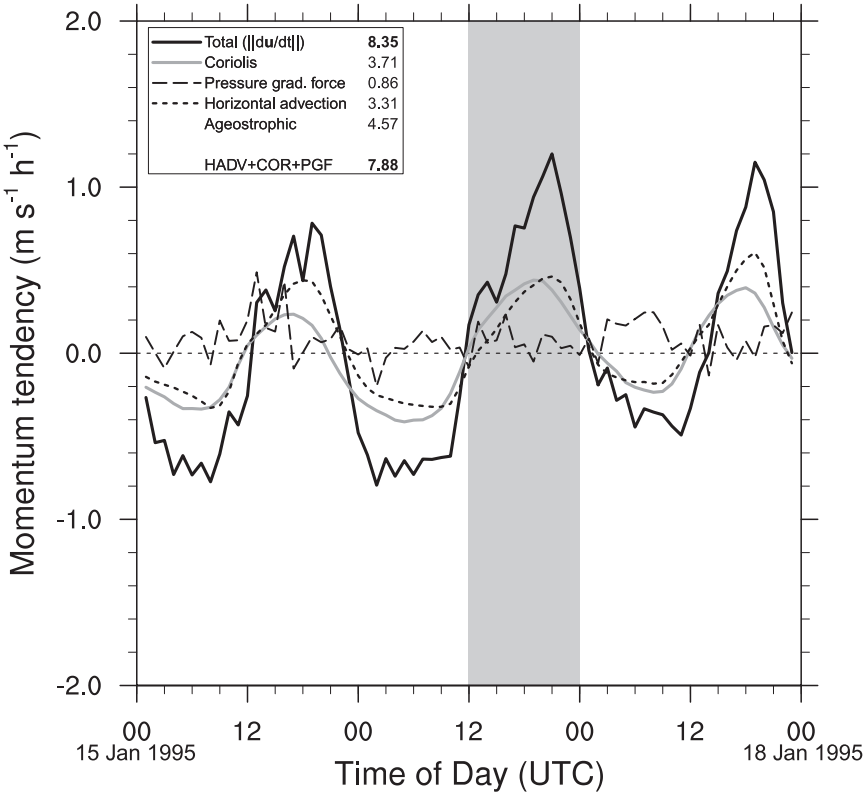

FIG. 13. As in Fig. 10, but for the Ethiopian NLLJ for 15–18 January 1995, averaged over the acceleration region denoted by the gray lines in Fig. 12b. The vertical gray bar bounds the times of the plan view plots in Figs. 12a,b.

over the 3 days shown. On 7 July, there are two maxima in the PGF. One occurs near 1000 UTC, which is about 4 h before sunset. The acceleration at this time does not match the sum of forces shown. The timing during mid-afternoon suggests that turbulent mixing perhaps negates the effect of PGF. A second peak in the PGF occurs just after sunset and coincides with the start of the acceleration of the nocturnal jet. The Coriolis force adds to the acceleration of the jet during this period. The positive contribution of PGF and Coriolis force to the acceleration on the first day differs from the results in Zhong et al. (1996) for the Great Plains NLLJ, wherein the nocturnal acceleration was dominated by the Coriolis force. On subsequent days, the Coriolis force dominates the variability of domain-averaged accelerations along the southern flank of the Tian Shan mountains.

The transience of the pattern is evident in the time series for subsequent days. Northerly flow becomes more pronounced and more nearly geostrophic. There continues to be a nightly westward acceleration, but the overall strength of the easterly jet decreases. Northwesterlies begin to dominate, associated with downslope flow in the lee of the Tian Shan mountains and removal of cold air at the entrance to the Tarim Basin.

The third example of a NLLJ is found over western Ethiopia (site 17 in Fig. 4b). This jet occurs in Northern Hemisphere winter, although the latitude is around 10°N. The major topographic feature of the region is the Ethiopian Highlands, which extend to about 3000 m MSL (Fig. 11a). The composite analysis during the time of maximum nocturnal jet strength indicates that the north-northeasterly jet forms as easterly flow traverses the northern slopes of the highlands (Fig. 11b) and a vortex forms in the lee. This jet rapidly accelerates around 2100 LT (Fig. 11d) and lasts through the night (Figs. 11d, 12c). The Ethiopian jet rapidly decelerates after sunrise.

The momentum budget for the Ethiopian jet at 900 hPa (Fig. 13) shows a predominately diurnal behavior in the Coriolis and advection terms, but not in the PGF term. The PGF is directed normal to the developing jet (not shown). As the elevated heating associated with the Ethiopian Highlands begins, air accelerates southeastward toward the mountains and gradually turns southwestward because of the Coriolis force. Horizontal

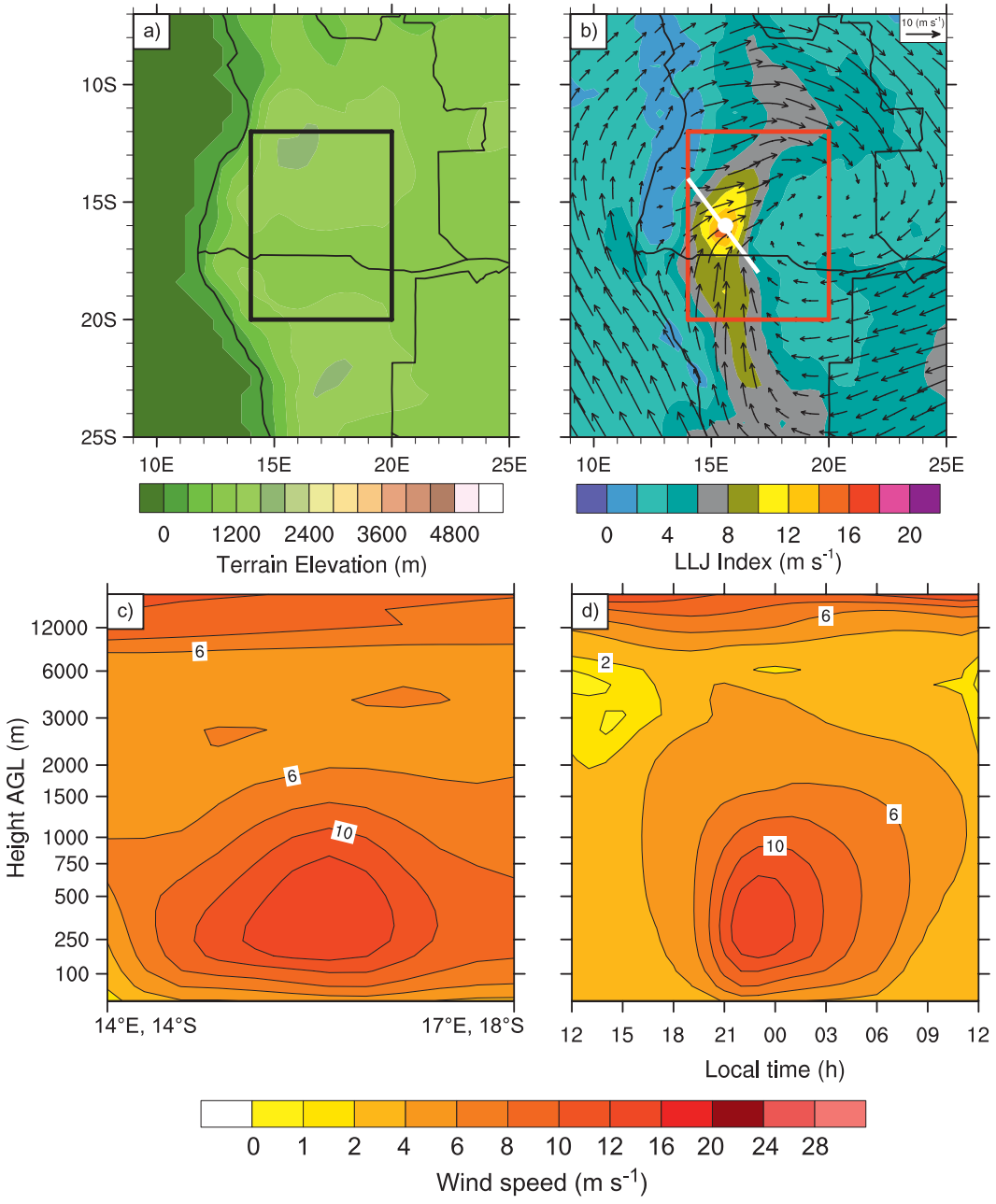

FIG. 14. As in Fig. 7, but for the Namibia NLLJ for January 1985–2005 (site 15 in Fig. 4b).

advection is also important in this case. North of the averaging box, the wind remains northeasterly, and the northeasterlies progress southward into the box during the evening.

Alternatively, one can view the jet as resulting from the formation of a cyclonic lee vortex on the west side of the Ethiopian Highlands (Figs. 11b, 12b). The general character of partially blocked flow is clear from the splitting of easterlies around the highlands (Figs. 11b, 12a,b). The lee vortex is evident in the lee of the northern flank of the highlands. A similar nocturnal vortex mechanism was discussed by Davis et al. (2000) in the context of lee vortices in the bight region of California. The single cyclonic vortex is characteristic of the response to large mountains (Boyer et al. 1987; Peng et al. 1995) where the Rossby number (U/fL) is less than or of order unity. The term Ro in the present case, with L the cross-flow length scale of the topography, is about unity (for $L = 500$ km, $f = 2.5 \times 10^{-5}$ s^{-1}, and $U = 10$ m s^{-1}). At moderate Ro (and low Froude number), the effects of rotation are

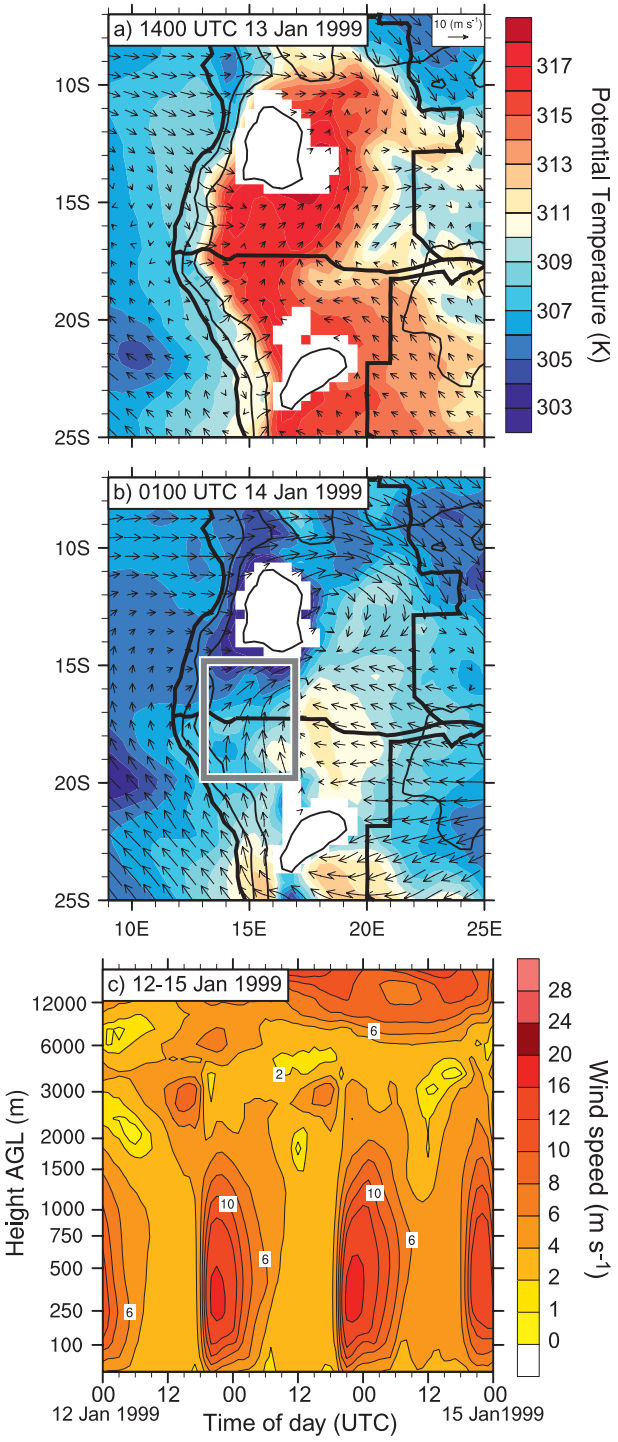

FIG. 15. As in Fig. 9, but for the Namibia NLLJ for a multiday episode during 12–15 January 1999. Time–height plot is for the jet core whose position is denoted by the white circle in Fig. 14b. Vector winds are plotted at approximately every second grid point.

important even though the region is relatively near the equator. Vortex formation in this case is clearly modified by surface heating, which causes a strong return flow in the lee to develop (Reisner and Smolarkiewicz 1994) and later adjusts geostrophically as mentioned earlier.

The NLLJ over Namibia and Angola (site 15 in Fig. 4b) occurs broadly within the strong land–sea temperature contrast that develops during the day in the warm season (January). Other areas of the world along the west coast of continents are also susceptible to similar coast-parallel jets that develop in the evening (Fig. 4). The average structure of the jet indicates a maximum frequency over southern Angola about 300 km inland from the Atlantic coast (Fig. 14b). The vertical structure reveals a maximum jet speed of about 14 m s^{-1} at an altitude of 300–400 m AGL (Fig. 14c). The onset of the jet is abrupt, at around 2000–2100 LT (Fig. 14d). This jet has a somewhat shorter temporal extent than the Ethiopian jet.

Topographic variations along the coast exert a profound influence on the structure of the nocturnal winds in the Namibia–Angola NLLJ (Fig. 14a). First, there is a coastal escarpment that rises to about 1 km MSL and roughly maintains this altitude far into the continent's interior. This plateau represents the westward reach of the Kalahari Desert and experiences extreme heating during the daytime, which accentuates the horizontal temperature contrast from the marine air (Fig. 15a), in this particular case from January 1999. The afternoon temperature contrast on the 850-hPa surface is roughly 10°C over a distance of about 150 km in the analyses.

The momentum budget (Fig. 16) reveals that all forcing terms oscillate diurnally. The development of the Namibian jet is particularly rapid, as indicated by the sharp spike in the wind tendency term (see also Fig. 15c). The Coriolis and advection terms together are the dominant contributions to the jet formation. However, the pressure gradient force associated with the afternoon land–sea contrast is also very large (not shown), but the force is directed approximately normal to the direction of the developing jet. The Coriolis acceleration represents a turning of westerly flow toward the north. The advection term represents the import of northward momentum through the southern boundary of the box. This flow, in turn, results from a slightly earlier inland push of marine air that is rotated by the Coriolis force as well. The abrupt onset of the jet results from the rapid import of southerly momentum into the box. The overall budget indicates a slight excess of momentum forcing compared to realized acceleration. This is consistent with the assumed influence of friction and turbulent mixing over the plateau. Unlike the Tarim Pendi case, there is apparently no phase lag between forcing terms and the acceleration.

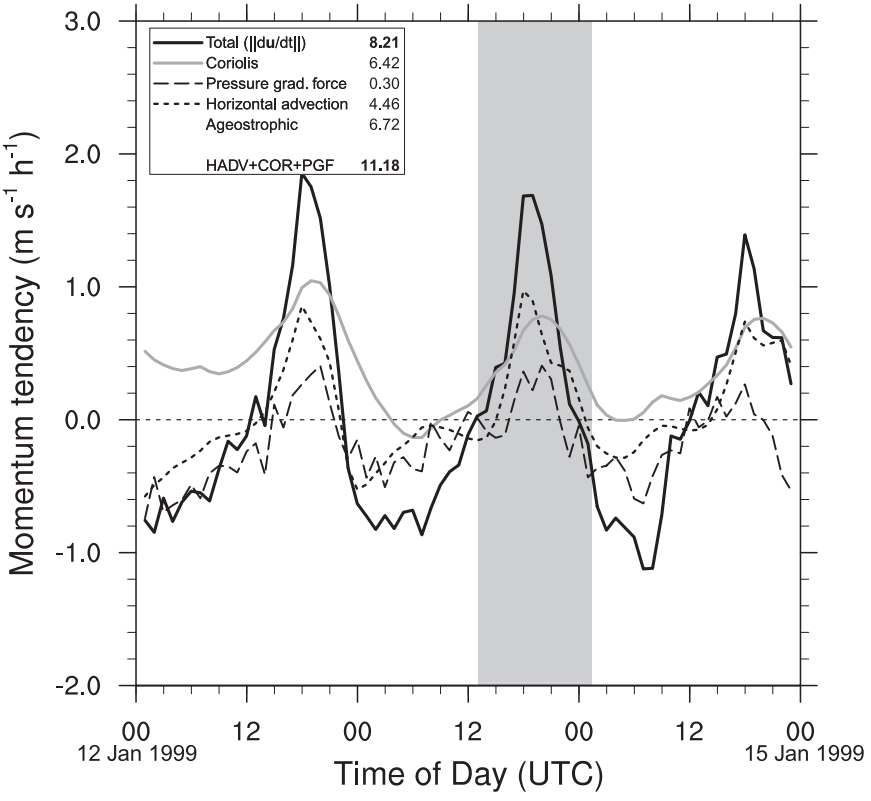

FIG. 16. As in Fig. 10, but for the Namibia NLLJ for 12–15 January 1999, averaged over the acceleration region denoted by the gray lines in Fig. 15b. The vertical gray bar bounds the times of the plan view plots in Figs. 15a,b.

6. Summary and commentary

This study has documented the characteristics of diurnally varying LLJs, ubiquitous features within the world's land-covered areas that strongly drive the regional climate. To accomplish our goal, we developed a 21-yr global downscaled reanalysis using NCAR's CFDDA, an MM5- and WRF-based climate downscaling system. The uniqueness of this dataset is its hourly three-dimensional output, which allows us to fully resolve the diurnal cycle for any point on the globe. Moreover, CFDDA's 40-km grid spacing better resolves many of the physiographic features that drive the regional weather and climate compared to other widely available global reanalyses. As we have shown, CFDDA largely replicates the diurnal variations of the winds within the PBL, and in a companion paper we show that CFDDA resolves the diurnal cycle of precipitation.

The first quantitative global maps of NLLJs were created for this study, using a new index of NLLJ activity that is based on the vertical structure of the wind's temporal variation. A database of daily NLLJ index values for the entire 21-yr period was generated and then used to form composite global maps of NLLJ activity that highlight not only the locations for recurring jets, but also their mean strength and direction, horizontal extent, geographic orientation, and amplitude of diurnal variation. This technique was shown to resolve not only all the known NLLJs reported in S96, but also a number of newly identified jets. The new NLLJs include those recurring over Ethiopia, Venezuela, Guyana, Syria, Iran, Tarim Pendi, Tibet, the Brazilian Highlands, and the Great Rift Valley in Africa. Our analysis indicates that NLLJs tend to be at their maxima near local midnight with the height of the jet core ranging from 300 to 600 m AGL. The diurnal cycle of the jets varied greatly from location to location. The orientation of NLLJs included all four primary directions (north, south, east, and west), with the mean direction in each region depending strongly on the geographic orientation of the adjacent physiography and the underlying horizontal heat contrasts. Three of the many newly identified NLLJs were described in detail, each caused by comparatively unique forcing mechanisms; these included jets in Tarim Pendi in northwest China, Ethiopia in eastern Africa, and Namibia–Angola in southwest Africa.

This study, along with the companion paper of Monaghan et al. (2010), shows that NLLJs have a profound influence on the regional climate. In many locations, they transport copious moisture, whereas in others they may loft and transport dust over long distances (Todd et al. 2008; Zunckel et al. 1996). Jets responsible for transporting moisture have a large impact on the hydrologic cycle. For example, the study by Byerle and Paegle (2003) suggested that enhanced cross-mountain upper-level zonal flow over the Rocky Mountains in the western United States influences the Great Plains NLLJ by accentuating the hydrologic cycle over the upper Mississippi River basin and likely contributed to severe rainfall and devastating flooding in that region during the summer of 1993. Dust transported by NLLJs may also have far-reaching impacts on climate and human health. One noteworthy example is the lofting of large quantities of dust in the Sahara (e.g., Washington et al. 2003; Engelstaedter and Washington 2007). Atmospheric mineral-dust loading is one of the largest uncertainties in global climate-change modeling and is known to have a significant impact on the radiation budget and cloud microphysics. The strong NLLJ activity identified in this study over the Sahara in North Africa may play a role in long-range dust transport.

To conclude, although the basic mechanisms of NLLJ formation have been understood for more than 40 years, the actual phenomenology of low-level jets is remarkably varied and much of this variety has escaped scrutiny until now. Horizontal heating contrasts, synoptic-scale transients, and diurnal changes in boundary layer turbulence combine to produce this rich variety of flow features. Most regions of the tropics or warm-season extratropics experience NLLJs on a regular basis. Furthermore, these jets have mesoscale and synoptic-scale extent. This implies that coherent transport can occur on scales of hundreds of kilometers overnight. The shallowness of the jets, their dependence on turbulence, and their ubiquity and intensity underscore a fundamental challenge to global weather and climate modeling of the distribution of atmospheric constituents originating from the earth's surface and human activity.

Acknowledgments. This research was funded by the Defense Threat Reduction Agency through an Interagency Agreement with the National Science Foundation. We gratefully acknowledge Andrea Hahmann (NCAR) for her work on the CFDDA land surface model and GLDAS data retrieval and processing. We also thank Tom Warner (NCAR) for reviewing an early version of the manuscript and the two anonymous reviewers for helping us to improve the final manuscript. The SALLJEX PIBAL data were obtained from the U.S. National Severe Storms Laboratory, and the NPN data were obtained from the NCAR Research Data Archive. The ERA-Interim data were obtained from the European Center for Medium-Range Weather Forecasting Data Server.

APPENDIX

Global Version of CFDDA

a. Basic CFDDA model configuration

The configuration of the MM5-based CFDDA system is summarized in Table 1; details about special model characteristics can be found in Grell et al. (1995). Before creating the 21-yr reanalysis for this study, we performed a number of sensitivity experiments designed to identify the physical process parameterizations that provide maximum numerical stability, and for producing the best possible representation of the mean structure and statistical behavior of the atmosphere within the boundary layer.

b. Global coverage with composite meshes

The global version of CFDDA implemented for this study employs composite meshes to cover the sphere (Williamson 2007). Twin polar stereographic computational grids are used, one centered over each pole and extending slightly beyond the equator. The domains overlap the equator by a sufficiently large amount, such that the zone where the grids are joined via simple interpolation straddles the equator. The terrain elevation and land use for both grids is made identical at coincident points within the equatorial interface, to avoid vertical and horizontal inconsistencies across the grids. Our approach follows that of Dudhia and Bresch (2002); however, instead of directly linking the grids during the simulation, they are integrated separately for each hourly output time and then joined at the equatorial interface using a Cressman-type interpolation function. The solution for grid points that lie more than 3° beyond the equator and into the opposite hemisphere is discarded. This represents a waste of about 20% of the computations in each grid. Apart from the small loss of computational efficiency, the composite mesh approach has been shown to be as good as spectral methods (Browning et al. 1989). Consistent with the findings of Dudhia and Bresch (2002), our tests of the grid configuration showed no sign of the equatorial interface in features moving across the equator. Moreover, we have seen no evidence of such features in the 21-yr downscaled analysis.

c. Initial and lateral boundary conditions

Individual simulations are reinitialized every 8.5 days, using the large-scale (2.5° × 2.5° grid) NR2 (Kanamitsu

et al. 2002). Although the rationale for the cold starts is that they prevent the accumulation of error in data-sparse areas, there has been no evidence of this problem. Each simulation overlaps the previous one by 24 h to avoid using output during the model spinup period. Qian et al. (2003) and Lo et al. (2008) recommend this approach. An added advantage of segmenting the simulation is that it allows for simultaneous integrations for different time periods. The NR2 analyses are also used to calculate the lateral boundary conditions and to preserve consistency between the large-scale features in the NR2 and CFDDA.

Initial land surface conditions are based on the National Aeronautics and Space Administration (NASA) Global Land Data Assimilation System (GLDAS; Rodell et al. 2004) dataset that is defined on a ($1.0° \times 1.0°$) grid. The GLDAS fields used here are substrate soil moisture and temperature at depths of 10 and 200 cm, ground skin temperature, and snow water equivalent. These fields are interpolated to all land grid points on each CFDDA hemispheric grid and replace the standard values defined in the NR2 analysis. Because the same land surface scheme is used in both GLDAS and CFDDA, no soil moisture conversion is required. Sea surface temperatures (SSTs) are interpolated to CFDDA ocean grid points on each model domain using the NCEP global optimum interpolation SST (OISST) dataset (Reynolds et al. 2002) that is defined on a ($0.25° \times 0.25°$) grid and updated daily.

d. Data assimilation technique

Data assimilation by Newtonian relaxation is accomplished by adding nonphysical nudging terms to the model predictive equations (Stauffer et al. 1991; Stauffer and Seaman 1994; Seaman et al. 1995; Fast 1995). These terms force the model solution at each grid point to standard surface and upper-air observations, in proportion to the difference between the model solution and the data. This approach is used because it is computationally efficient, it is robust, it allows the model to ingest data continuously rather than intermittently, the full model dynamics are part of the assimilation system so that analyses contain all locally forced mesoscale features, and it does not unduly complicate the structure of the model code. With observation nudging, each observation is ingested into the model at its observed time and location, with proper space and time weights, and the model spreads the information in time and space according to the model dynamics. In addition, the observational values undergo a rigorous quality control as described by Liu et al. (2004).

For this study, we use a combination of nudging toward the observations (observation nudging) and nudging toward the driving NR2 analysis (grid nudging). Although both techniques are used to continuously steer the CFDDA analyses toward the true state of the atmosphere, the grid nudging scheme is designed to be maximally effective on the larger scales without effecting the solution of smaller-scale features. Thus, the observations and CFDDA provide small-scale atmospheric information, particularly within the PBL, whereas the NR2 preserves the large-scale state in CFDDA at upper levels and also ensures mass conservation. A time-invariant vertical grid nudging zone is used, from the model top down to about 3.0 km AGL (above the average height of the PBL). The magnitude of the grid nudging coefficients is objectively determined by examining the spectral response on the CFDDA solution to progressively weaker coefficients. The idea is for the CFDDA large-scale solution to closely follow that of the NR2 while not impeding the ability of the assimilated observations and CFDDA to produce regional and small-scale features, especially within the PBL. This approximates the spectral nudging technique, wherein nudging is applied to wavelengths of the regional model solution at or above a prescribed threshold and only within the upper levels (e.g., von Storch et al. 2000; Kanamaru and Kanamitsu 2007; Alexandru et al. 2009).

REFERENCES

Alexandru, A., R. de Elia, R. Laprise, L. Separovic, and S. Biner, 2009: Sensitivity study of regional climate model simulations to large-scale nudging parameters. *Mon. Wea. Rev.,* **137,** 1666–1686.

Blackadar, A. K., 1957: Boundary layer wind maxima and their significance for the growth of nocturnal inversions. *Bull. Amer. Meteor. Soc.,* **38,** 283–290.

Bonner, W. D., 1968: Climatology of the low level jet. *Mon. Wea. Rev.,* **96,** 833–850.

Boyer, D. L., P. A. Davies, W. R. Holland, F. Biolley, and H. Honji, 1987: Stratified rotating flow over and around isolated three-dimensional topography. *Philos. Trans. Roy. Soc. London,* **322A,** 213–241.

Browning, G. L., J. J. Hack, and P. N. Swartztrauber, 1989: A comparison of three numerical methods for solving differential equations on the sphere. *Mon. Wea. Rev.,* **117,** 1058–1075.

Byerle, L. A., and J. Paegle, 2003: Modulation of the Great Plains low-level jet and moisture transports by orography and large-scale circulations. *J. Geophys. Res.,* **108,** 8611, doi:10.1029/2002JD003005.

Carbone, R. E., and J. D. Tuttle, 2008: Rainfall occurrence in the U.S. warm season: The diurnal cycle. *J. Climate,* **21,** 4132–4146.

Chen, F., and J. Dudhia, 2001a: Coupling an advanced land-surface/hydrology model with the Penn State/NCAR MM5 modeling system. Part I: Model implementation and sensitivity. *Mon. Wea. Rev.,* **129,** 569–585.

——, and ——, 2001b: Coupling an advanced land-surface/hydrology model with the Penn State/NCAR MM5 modeling system. Part II: Model validation. *Mon. Wea. Rev.,* **129,** 587–604.

Daniel, C. J., R. W. Arritt, and C. J. Anderson, 1999: Accuracy of 404-MHz radar profilers for detection of low-level jets over the central United States. *J. Appl. Meteor.,* **38,** 1391–1396.

Darby, L. S., K. J. Allwine, and R. M. Banta, 2006: Nocturnal low-level jet in a mountain basin complex. Part II: Transport and diffusion of tracer under stable conditions. *J. Appl. Meteor. Climatol.,* **45,** 740–753.

Davis, C., S. Low-Nam, and C. Mass, 2000: Dynamics of a Catalina eddy revealed by numerical simulation. *Mon. Wea. Rev.,* **128,** 2885–2904.

Doyle, J. D., and T. T. Warner, 1993: A three-dimensional investigation of a Carolina low-level jet during GALE IOP 2. *Mon. Wea. Rev.,* **121,** 1030–1047.

Dudhia, J., 1989: Numerical study of convection observed during the winter monsoon experiment using a mesoscale two-dimensional model. *J. Atmos. Sci.,* **46,** 3077–3107.

——, and J. F. Bresch, 2002: A global version of the PSU–NCAR Mesoscale Model. *Mon. Wea. Rev.,* **130,** 2989–3007.

Engelstaedter, S., and R. Washington, 2007: Atmospheric controls on the annual cycle of North African dust. *J. Geophys. Res.,* **112,** D03103, doi:10.1029/2006JD007195.

Fast, J. D., 1995: Mesoscale modeling and four-dimensional data assimilation in areas of highly complex terrain. *J. Appl. Meteor.,* **34,** 2762–2782.

Grell, G. A., J. Dudhia, and D. R. Stauffer, 1995: A description of the fifth-generation Penn State/NCAR Mesoscale Model (MM5). NCAR Tech. Note NCAR/TN-398, 128 pp.

Hahmann, A. N., D. Rostkier-Edelstein, T. T. Warner, Y. Liu, F. Vandenberghe, Y. Liu, R. Babarsky, and S. P. Swerdlin, 2010: A reanalysis system for the generation of mesoscale climatographies. *J. Appl. Meteor. Climatol.,* **49,** 954–972.

Helfand, H. M., and S. D. Schubert, 1995: Climatography of the Great Plains low-level jet and its contribution to the continental moisture budget of the United States. *J. Climate,* **8,** 784–806.

Hering, W. S., and T. R. Borden, 1962: Diurnal variations in the summer wind field over the central United States. *J. Atmos. Sci.,* **19,** 81–86.

Higgins, R. W., Y. Yao, E. S. Yarosh, J. E. Janowiak, and K. C. Mo, 1997: Influence of the Great Plains low-level jet on summertime precipitation and moisture transport over the central United States. *J. Climate,* **10,** 481–507.

Hoecker, W. H., 1965: Comparative physical behavior of southerly boundary-layer wind jets. *Mon. Wea. Rev.,* **93,** 133–144.

Holton, J. R., 1967: The diurnal boundary layer wind oscillation above sloping terrain. *Tellus,* **19,** 199–205.

Hong, S.-Y., and H.-L. Pan, 1996: Nonlocal boundary layer vertical diffusion in a medium-range forecast model. *Mon. Wea. Rev.,* **124,** 2322–2339.

Jiang, X., N. C. Lau, I. M. Held, and J. J. Ploshay, 2007: Mechanisms of the Great Plains low-level jet as simulated in an AGCM. *J. Atmos. Sci.,* **64,** 532–547.

Kain, J. S., 2004: The Kain–Fritsch convective parameterization: An update. *J. Appl. Meteor.,* **43,** 170–181.

Kanamaru, H., and M. Kanamitsu, 2007: Scale-selective bias correction in a downscaling of global analysis using a regional model. *Mon. Wea. Rev.,* **135,** 334–350.

Kanamitsu, M., W. Ebisuzaki, J. Woollen, S.-K. Yang, J. J. Hnilo, M. Fiorino, and G. L. Potter, 2002: NCEP–DOE AMIP-II Reanalysis (R-2). *Bull. Amer. Meteor. Soc.,* **83,** 1631–1643.

Koren, I., Y. J. Kaufman, R. Washington, M. C. Todd, Y. Rudich, V. J. Martins, and D. Rosenfeld, 2006: The Bodélé depression—A single spot in the Sahara that provides most of the mineral dust to the Amazon forest. *Environ. Res. Lett.,* **1,** 1–5.

Liu, Y., F. Vandenberghe, S. Low-Nam, T. T. Warner, and S. Swerdlin, 2004: Observation-quality estimation and its application in the NCAR/ATEC real-time FDDA and forecast (RTFDDA) system. Preprints, *20th Conf. on Weather Analysis and Forecasting and 16th Conf. on Numerical Weather Prediction,* Seattle, WA, Amer. Meteor. Soc., J1.7. [Available online at http://ams.confex.com/ams/pdfpapers/71934.pdf.]

——, and Coauthors, 2008: The operational mesogamma-scale analysis and forecast system of the U.S. Army Test and Evaluation Command. Part I: Overview of the modeling system, the forecast products, and how the products are used. *J. Appl. Meteor. Climatol.,* **47,** 1077–1092.

Lo, J. C.-F., Z.-L. Yang, and R. A. Pielke Sr., 2008: Assessment of three dynamical downscaling methods using the Weather Research and Forecasting (WRF) model. *J. Geophys. Res.,* **113,** D09112, doi:10.1029/2007JD009216.

Mao, H., and R. Talbot, 2004: Role of meteorological processes in two New England ozone episodes during summer 2001. *J. Geophys. Res.,* **109,** D20305, doi:10.1029/2004JD004850.

Martner, B. E., and Coauthors, 1993: An evaluation of wind profiler, RASS, and microwave radiometer performance. *Bull. Amer. Meteor. Soc.,* **74,** 599–613.

Miller, P. A., M. F. Barth, J. R. Smart, and L. A. Benjamin, 1997: The extent of bird contamination in the hourly winds measured by the NOAA profiler network: Results before and after implementation of the new bird contamination quality control check. *Proc. First Symp. on Integrated Observing Systems,* Long Beach, CA, Amer. Meteor. Soc., 138–144.

Mitchell, M. J., R. W. Arritt, and K. Labas, 1995: A climatology of the warm season Great Plains low-level jet using wind profiler observations. *Wea. Forecasting,* **10,** 576–591.

Mlawer, E. J., S. J. Taubman, P. D. Brown, M. J. Iacono, and S. A. Clough, 1997: Radiative transfer for inhomogeneous atmospheres: RRTM, a validated k-correlated model for the longwave. *J. Geophys. Res.,* **102,** 16 663–16 682.

Mo, K. C., and E. H. Berbery, 2004: Low-level jets and the summer precipitation regimes over North America. *J. Geophys. Res.,* **109,** D06117, doi:10.1029/2003JD004106.

Monaghan, A. J., D. L. Rife, J. O. Pinto, C. A. Davis, and J. R. Hannan, 2010: Global precipitation extremes associated with diurnally varying low-level jets. *J. Climate,* **23,** 5065–5084.

Neiman, P. J., F. M. Ralph, G. A. Wick, Y. H. Kuo, T. K. Wee, Z. Ma, G. H. Taylor, and M. D. Dettinger, 2008: Diagnosis of an intense atmospheric river impacting the Pacific Northwest: Storm summary and offshore vertical structure observed with COSMIC Satellite retrievals. *Mon. Wea. Rev.,* **136,** 4398–4420.

Newell, R. E., N. E. Newell, Y. Zhu, and C. Scott, 1992: Tropospheric rivers?—A pilot study. *Geophys. Res. Lett.,* **19,** 2401–2404.

Nogués-Paegle, J., and K. C. Mo, 1997: Alternating wet and dry conditions over South America during summer. *Mon. Wea. Rev.,* **125,** 279–291.

Peng, M. S., S.-W. Li, S. W. Chang, and R. T. Williams, 1995: Flow over mountains: Coriolis force, transient troughs and three dimensionality. *Quart. J. Roy. Meteor. Soc.,* **121,** 593–613.

Qian, J. H., A. Seth, and S. Zebiak, 2003: Reinitialized versus continuous simulations for regional climate downscaling. *Mon. Wea. Rev.,* **131,** 2857–2874.

Ralph, F. M., P. J. Neiman, and G. A. Wick, 2004: Satellite and CALJET aircraft observations of atmospheric rivers over the eastern North Pacific Ocean during the winter of 1997/98. *Mon. Wea. Rev.,* **132,** 1721–1745.

——, ——, and R. Rotunno, 2005: Dropsonde observations in low-level jets over the northeastern Pacific Ocean from

CALJET-1998 and PACJET-2001: Mean vertical-profile and atmospheric-river characteristics. *Mon. Wea. Rev.,* **133,** 889–910.

Reisner, J. M., and P. K. Smolarkiewicz, 1994: Thermally forced low Froude number flow past three-dimensional obstacles. *J. Atmos. Sci.,* **51,** 117–133.

——, R. M. Rasmussen, and R. T. Bruintjes, 1998: Explicit forecasting of supercooled liquid water in winter storms using the MM5 forecast model. *Quart. J. Roy. Meteor. Soc.,* **124,** 1071–1107.

Reynolds, R. W., N. A. Rayner, T. M. Smith, D. C. Stokes, and W. Q. Wang, 2002: An improved in situ and satellite SST analysis for climate. *J. Climate,* **15,** 1609–1625.

Rodell, M., and Coauthors, 2004: The Global Land Data Assimilation System. *Bull. Amer. Meteor. Soc.,* **85,** 381–394.

Rotunno, R., 1983: On the linear theory of land and sea breeze. *J. Atmos. Sci.,* **40,** 1999–2009.

Salio, P., M. Nicolini, and E. J. Zipser, 2007: Mesoscale convective systems over southeastern South America and their relationship with the South American low-level jet. *Mon. Wea. Rev.,* **135,** 1290–1309.

Seaman, N. L., D. R. Stauffer, and A. M. Lario-Gibbs, 1995: A multiscale four-dimensional data assimilation system applied in the San Joaquin Valley during SARMAP. Part I: Modeling design and basic performance characteristics. *J. Appl. Meteor.,* **34,** 1739–1761.

Simmons, A., S. Uppala, D. Dee, and S. Kobayashi, 2007: The ERA interim reanalysis. *ECMWF Newsletter,* No. 110, ECMWF, Reading, United Kingdom, 25–35.

Skamarock, W. C., J. B. Klemp, J. Dudhia, D. O. Gill, D. M. Barker, W. Wang, and J. G. Powers, 2005: A description of the Advanced Research WRF version 3. National Center for Atmospheric Research Tech. Note NCAR/TN-468+STR, 100 pp.

Smith, B. L., S. E. Yuter, P. J. Neiman, and D. E. Kingsmill, 2009: Water vapor fluxes and orographic precipitation over Northern California associated with a land-falling atmospheric river. *Mon. Wea. Rev.,* **138,** 74–100.

Stauffer, D. R., and N. L. Seaman, 1994: Multiscale four-dimensional data assimilation. *J. Appl. Meteor.,* **33,** 416–434.

——, ——, and F. S. Binkowski, 1991: Use of four-dimensional data assimilation in a limited-area mesoscale model. Part II: Effects of data assimilation within the planetary boundary layer. *Mon. Wea. Rev.,* **119,** 734–754.

Stensrud, D. J., 1996: Importance of low-level jets to climate: A review. *J. Climate,* **9,** 1698–1711.

Todd, M. C., R. Washington, S. Raghavan, G. Lizcano, and P. Knippertz, 2008: Regional model simulations of the Bodélé low-level jet of northern Chad during the Bodele Dust Experiment (BoDEx 2005). *J. Climate,* **21,** 995–1012.

Tuttle, J., and C. A. Davis, 2006: Corridors of warm-season precipitation in the central United States. *Mon. Wea. Rev.,* **134,** 2297–2317.

Uppala, S. M., 2007: From ERA-15 to ERA-40 and ERA-Interim. *Proc. ECMWF–GEO Workshop on Atmospheric Reanalysis,* Reading, United Kingdom, ECMWF, 17–22.

van de Kamp, D. W., F. M. Ralph, M. F. Barth, P. A. Miller, J. R. Smart, and L. A. Benjamin, 1997: The new bird contamination quality control check applied to hourly winds from NOAA's profiler network. *Proc. 28th Conf. on Radar Meteorology,* Austin, TX, Amer. Meteor. Soc., 131–132.

Vera, C., and Coauthors, 2006: The South American Low-Level Jet Experiment. *Bull. Amer. Meteor. Soc.,* **87,** 63–77.

Vernekar, A. D., B. P. Kirtman, and M. J. Fennessy, 2003: Low-level jets and their effects on the South American summer climate as simulated by the NCEP Eta model. *J. Climate,* **16,** 297–311.

von Storch, H., H. Langenberg, and F. Feser, 2000: A spectral nudging technique for dynamical downscaling purposes. *Mon. Wea. Rev.,* **128,** 3664–3673.

Washington, R., M. Todd, N. J. Middleton, and A. S. Goudie, 2003: Dust-storm source areas determined by the total ozone monitoring spectrometer and surface observations. *Ann. Assoc. Amer. Geogr.,* **93,** 297–313.

——, M. C. Todd, S. Engelstaedter, S. M'Bainayel, and F. Mitchell, 2006: Dust and the low-level circulation over the Bodélé depression, Chad: Observations from BoDEx 2005. *J. Geophys. Res.,* **111,** D03201, doi:10.1029/2005JD006502.

Weber, B. L., and D. B. Wuertz, 1990: Comparison of rawinsonde and wind profiler radar measurements. *J. Atmos. Oceanic Technol.,* **7,** 157–174.

Whiteman, C. D., 2000: *Mountain Meteorology: Fundamentals and Applications*. Oxford University Press, 355 pp.

——, X. Bian, and S. Zhong, 1997: Low-level jet climatology from enhanced rawinsonde observations at a site in the Southern Great Plains. *J. Appl. Meteor.,* **36,** 1363–1376.

Williamson, D. L., 2007: The evolution of dynamical cores for global atmospheric models. *J. Meteor. Soc. Japan,* **85B,** 241–269.

Zhong, S., J. D. Fast, and X. Bian, 1996: A case study of the Great Plains low-level jet using wind profiler network data and a high-resolution mesoscale model. *Mon. Wea. Rev.,* **124,** 785–806.

Zunckel, M., G. Held, R. A. Preston-Whyte, and A. Joubert, 1996: Low-level wind maxima and the transport of pyrogenic products over southern Africa. *J. Geophys. Res.,* **101,** 23 745–23 755.